



OPEN ACCESS

EDITED BY

Sari E. Lauri,
University of Helsinki, Finland

REVIEWED BY

Tabrez Jamal Siddiqui,
University of Manitoba, Canada
Zhiping P. Pang,
Rutgers, The State University of New Jersey,
United States
Tak Pan Wong,
McGill University, Canada

*CORRESPONDENCE

Graham M. Pitcher
✉ graham.pitcher@sickkids.ca
Michael W. Salter
✉ michael.salter@sickkids.ca

RECEIVED 02 April 2023

ACCEPTED 16 June 2023

PUBLISHED 12 July 2023

CITATION

Pitcher GM, Garzia L, Morrissy AS, Taylor MD
and Salter MW (2023) Synapse-specific
diversity of distinct postsynaptic GluN2
subtypes defines transmission strength
in spinal lamina I.
Front. Synaptic Neurosci. 15:1197174.
doi: 10.3389/fnsyn.2023.1197174

COPYRIGHT

© 2023 Pitcher, Garzia, Morrissy, Taylor and
Salter. This is an open-access article distributed
under the terms of the [Creative Commons
Attribution License \(CC BY\)](#). The use,
distribution or reproduction in other forums is
permitted, provided the original author(s) and
the copyright owner(s) are credited and that
the original publication in this journal is cited,
in accordance with accepted academic
practice. No use, distribution or reproduction is
permitted which does not comply with
these terms.

Synapse-specific diversity of distinct postsynaptic GluN2 subtypes defines transmission strength in spinal lamina I

Graham M. Pitcher^{1,2*}, Livia Garzia³, A. Sorana Morrissy⁴,
Michael D. Taylor⁵ and Michael W. Salter^{1,2*}

¹Program in Neurosciences and Mental Health, The Hospital for Sick Children, Toronto, ON, Canada, ²Department of Physiology, University of Toronto, Toronto, ON, Canada, ³Department of Surgery, Faculty of Medicine, McGill University, and Cancer Research Program, The Research Institute of the McGill University Health Centre, Montreal, QC, Canada, ⁴Department of Biochemistry and Molecular Biology, Cumming School of Medicine, University of Calgary, Calgary, AB, Canada, ⁵Brain Tumor Program, Texas Medical Centre, Houston, TX, United States

The unitary postsynaptic response to presynaptic quantal glutamate release is the fundamental basis of excitatory information transfer between neurons. The view, however, of individual glutamatergic synaptic connections in a population as homogenous, fixed-strength units of neural communication is becoming increasingly scrutinized. Here, we used minimal stimulation of individual glutamatergic afferent axons to evoke single synapse resolution postsynaptic responses from central sensory lamina I neurons in an *ex vivo* adult rat spinal slice preparation. We detected unitary events exhibiting a NMDA receptor component with distinct kinetic properties across synapses conferred by specific GluN2 subunit composition, indicative of GluN2 subtype-based postsynaptic heterogeneity. GluN2A, 2A and 2B, or 2B and 2D synaptic predominance functioned on distinct lamina I neuron types to narrowly, intermediately, or widely tune, respectively, the duration of evoked unitary depolarization events from resting membrane potential, which enabled individual synapses to grade differentially depolarizing steps during temporally patterned afferent input. Our results lead to a model wherein a core locus of proteomic complexity prevails at this central glutamatergic sensory synapse that involves distinct GluN2 subtype configurations. These findings have major implications for subthreshold integrative capacity and transmission strength in spinal lamina I and other CNS regions.

KEYWORDS

NMDA receptor, glutamate, synapse, minimal stimulation, unitary, quantal, spinal cord, lamina I

Introduction

The unitary postsynaptic response to quantal glutamate release is the fundamental basis of excitatory information transfer in the central nervous system (CNS). The prevailing assumption that glutamatergic synaptic connections in a given neural network or population function as homogenous, equal strength relay units of excitatory information is beginning

to face critical re-evaluation (Grant and Fransén, 2020). The core components of a typical glutamatergic synapse include glutamate-gated ionotropic receptors (iGluRs) consisting primarily of α -amino-3-hydroxy-5-methyl-4-isoxazole propionate (AMPA) and N-methyl-D-aspartate glutamate receptor-channel (NMDAR) complexes, along with adhesion and signaling molecules (Frank and Grant, 2017; Zhu et al., 2018; Cizeron et al., 2020). However, there is increased scrutiny directed toward a more comprehensive understanding of postsynaptic molecular composition and assembly—do a multitude of postsynaptic receptor-channel and protein constituents occur as a generic mix across synapses in a population, or is there a molecular codification to their nanopositioning and function that tunes transmission strength at individual glutamatergic synapses?

Recent advances in single-cell RNA sequencing and proteomics in the rodent brain (Roy et al., 2018a,b; Zhu et al., 2018; Cizeron et al., 2020) and spinal cord (Häring et al., 2018; Broadhead et al., 2020) have identified considerable diversity in synaptic RNA and protein content. At glutamatergic synapses in particular, molecular complexity is reflected extensively in the postsynaptic density (PSD) portion (Collins et al., 2006; Coba et al., 2009; Zhu et al., 2018; Broadhead et al., 2020; Cizeron et al., 2020) where AMPA and NMDA receptors are optimally situated for synaptic function. Though the NMDAR multiprotein structure itself is composed exclusively of ion channel subunits consisting of a heterotetramer core comprised of two obligate GluN1 subunits and two GluN2 subunits (Paoletti et al., 2013), NMDARs contained within “NMDAR supercomplexes” (Frank et al., 2016; Frank and Grant, 2017) are bound to a myriad of adhesion and signaling binding partners (Frank et al., 2016, 2017; Frank and Grant, 2017). Notably, dissimilar GluN2 subunits of which four types exist (2A-D) (Paoletti et al., 2013) are subjected to differing interactions with distinct PSD proteins (Kornau et al., 1995; Bassand et al., 1999; Valtschanoff et al., 1999; Losi et al., 2003; Lin et al., 2004; Gardoni and Di Luca, 2021) including for example PSD-95 (Cousins et al., 2008, 2009; Bard et al., 2010; Cousins and Stephenson, 2012) indicative of GluN2 subtype regulation by distinct PSD binding partners. Although there is compelling evidence that NMDARs congregate in a cluster primarily at the center of the PSD (Kharazia and Weinberg, 1997; Chen et al., 2015; Goncalves et al., 2020), recent progress *in vitro* using single-molecule and super-resolution imaging in cultured hippocampal neurons has now identified more precise spatial organization of distinct GluN2 subtypes in defined nanodomains in the PSD with the localization of each determined individually by specific PSD binding partners within the NMDAR supercomplex (Kellermayer et al., 2018; Hruska et al., 2022). The known extensive complexity of PSD protein constituents (Frank and Grant, 2017; Roy et al., 2018b; Cizeron et al., 2020) and the regulatory function they impose on GluN2 subtype nanoscale localization *in vitro* (Kellermayer et al., 2018; Hruska et al., 2022) therefore open the potential for multiple scenarios of diverse GluN2 subtype(s) organization within the PSD compartment. However, our current understanding of GluN2 subtype diversity and distinct PSD compartmentalization at the resolution of individual synapses in higher-order mammalian synaptic circuits or populations remains elusive. Moreover, though GluN2 subunit composition within the NMDAR complex is known to determine several biophysical receptor-channel properties that mediate current flow (Clarke and Johnson, 2006;

Siegler Retchless et al., 2012), the functional significance that distinct GluN2 subtype localization within the PSD imposes on unitary integrative capacity and transmission strength at individual synapses remains unexplored. Limited consideration may be dedicated to these issues likely because of the technically challenging nature of investigating NMDARs, their properties, and function at single-synapse resolution in *in vivo* or *ex vivo* CNS preparations.

We set out here to understand GluN2 subtype organization and function at the resolution of individual mature mammalian glutamatergic synaptic connections using an electrophysiological approach. We developed a minimal stimulation protocol in an *ex vivo* adult rat spinal cord slice preparation in which we evoked unitary excitatory postsynaptic currents (μ EPSCs) and potentials (μ EPSPs) at individual synaptic connections between glutamatergic primary afferents (Broman et al., 1993; Broman and Adahl, 1994; Todd et al., 2003) in the dorsal rootlet and central neurons in the lamina I nociceptive subfield of the spinal dorsal horn, a major CNS somatosensory region. μ EPSCs exhibited distinctive NMDAR kinetic properties at this principal sensory synapse providing evidence supporting a high degree of diversity of single or multiple GluN2 subtype postsynaptic configurations at individual glutamatergic synaptic connections. μ EPSP recordings further identified distinct GluN2 subtype configurations as a fundamental single-synapse resolution coding mechanism. Our results support a model wherein the mature mammalian primary afferent-lamina I neuron glutamatergic synapse is a core locus of distinct GluN2 subtype-based proteome diversity and nanoscale organization that directly influences fundamental aspects of subthreshold transmission efficacy including unitary resolution synaptic computation capability and strength, and ultimately how somatosensory information is processed. In other CNS regions diverse postsynaptic GluN2 subunit composition may constitute distinct integrative signatures at glutamatergic synapses that bear major implications in physiological transmission strength and information transfer.

Results

Unitary primary afferent-lamina I neuron synaptic responses

To investigate NMDAR GluN2 subtypes at mature, lamina I synapses, we made whole-cell voltage-clamp recordings from visually identified lamina I neurons in acute *ex vivo* dorsal root-attached transverse spinal cord slices from adult rats. We elicited primary afferent-mediated post-synaptic responses in lamina I neurons by delivering single electrical stimuli to the attached dorsal rootlet. Stimulation of primary afferents synaptically connected to lamina I neurons evoked excitatory post-synaptic currents (EPSCs) (Figure 1A). When the membrane potential was held at hyperpolarized potentials, we observed a rapid-onset, rapidly decaying EPSC response. Holding the neuron at positive membrane potentials revealed a slowly decaying component of the EPSC, in addition to the rapid-onset peak. The peak of the rapid onset component exhibited a linear current-voltage relationship, whereas the slowly decaying EPSC component showed dramatic inward

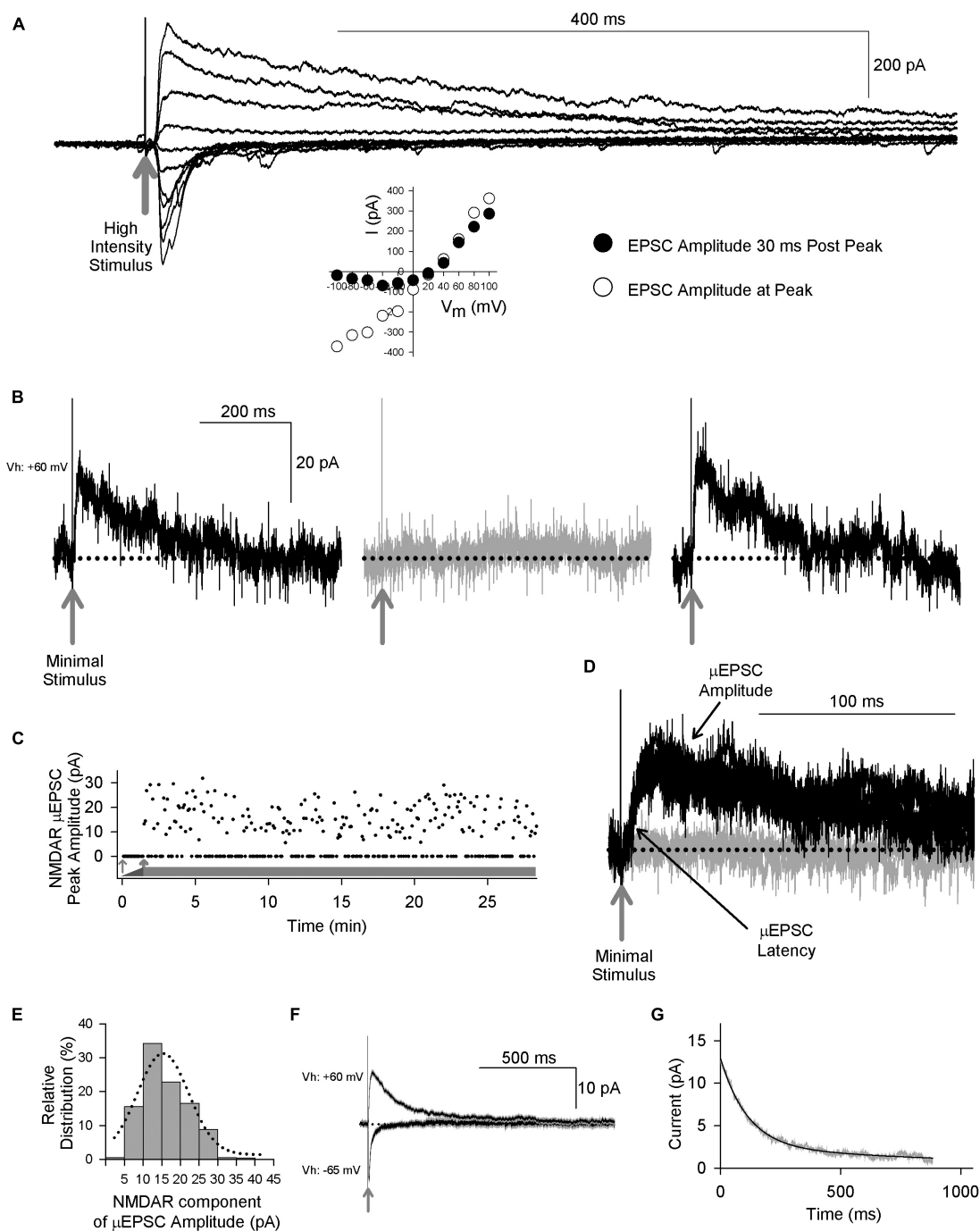


FIGURE 1

Primary afferent-evoked μ EPSCs in whole cell voltage-clamp recordings from lamina I neurons in acute *ex vivo* dorsal root-attached transverse spinal cord slices from adult rats exhibit kinetic properties of both AMPA and NMDARs. **(A)** Delivery of a single high intensity electrical stimulus (gray arrow indicates stimulus artifact) to the attached rootlet that activates multiple primary afferent axons evokes large amplitude EPSCs in a lamina I neuron. Stimulation at hyperpolarized membrane potentials elicits rapid onset, rapidly decaying EPSC responses, whereas stimulation at depolarizing membrane potentials evokes a slowly decaying component, in addition to the rapid-onset peak. Peak of the rapid onset component shows a linear current-voltage relationship (inset below, white symbols) consistent with kinetic properties of AMPARs, while the slowly decaying EPSC component shows inward rectification (inset below, black symbols) consistent with current-voltage (I-V) relationship of NMDARs. **(B)** Recordings of unitary-evoked EPSCs from a representative adult rat spinal lamina I neuron elicited by minimal stimulation of the attached dorsal rootlet. Sample traces showing individual consecutive all-or-none μ EPSCs held at +60 mV evoked by minimal stimulation. The black traces show successful synaptic μ EPSCs in response to minimal sensory afferent stimulation (gray arrow indicates stimulus artifact) while the gray trace shows a synaptic failure. **(C)** Scatter plot of successful synaptic μ EPSC responses and failures over time (thick gray bar) evoked by minimal stimulation (0.2 Hz). The thin gray arrow indicates subthreshold stimulation intensity while the thick gray arrow indicates threshold at which μ EPSCs can be evoked. **(D)** Several successful synaptic μ EPSCs (black traces) from the same recording in panel **(B)** showing identical amplitude and latency (black arrows) consistent with a monosynaptic connection (gray arrow indicates stimulus artifact). The gray trace indicates a synaptic failure. **(E)** NMDAR amplitude histogram showing relative distribution for successful μ EPSCs, fit with a single Gaussian function. **(F)** Averaged traces (\pm SEM) showing successful μ EPSCs held at +60 mV and from the same recording successful μ EPSCs held at -65 mV. **(G)** Single exponential fitting of the decay component of the averaged μ EPSC held at +60 mV.

rectification (Figure 1A). The rapid-onset component of the EPSC was blocked by the AMPAR antagonist CNQX and the slow component was blocked by the NMDAR competitive antagonist D-amino-phosphonovaleric acid (D-APV, 100 μ M; not illustrated). Thus, adult lamina I dorsal horn neurons exhibit primary afferent-evoked EPSCs with kinetic and pharmacological properties of both AMPA and NMDA receptors.

To examine individual primary afferent-evoked EPSCs of lamina I neurons in the dorsal root-attached spinal cord slice preparation we used a minimal stimulation protocol (Hildebrand et al., 2014) to evoke unitary, monosynaptic EPSCs (μ EPSCs) in the lamina I neuron recorded ($n = 224$ cells). The criteria used to establish monosynaptic μ EPSC responses were: a distinct electrical stimulation threshold at which responses were all-or-none (i.e., success or failure; Figures 1B, C), a consistent latency throughout the duration of each recording (Figure 1D), and the amplitude of the NMDAR component was normally distributed (Figure 1E). We confirmed that responses evoked by the minimal stimulation were *bona fide* unitary responses because increasing stimulus intensity did not increase μ EPSC amplitude until the intensity was sufficient to evoke a second level of all-or-none evoked responses (Supplementary Figure 1C). Moreover, bath-applying tetrodotoxin (TTX) to block voltage-gated Na^+ channels eliminated the μ EPSCs (Supplementary Figures 1A, B), indicating that unitary synaptic responses were driven by action potentials evoked by direct stimulation of a presynaptic axon in the dorsal rootlet rather than by direct focal stimulation of the lamina I neuron.

To determine whether or not the response failures with minimal stimulation were due to failure of the stimulating electrode to generate an action potential in the primary afferent axon in the dorsal rootlet eliciting the μ EPSC, we used paired-pulse minimal stimulation experiments (Supplementary Figures 1D, E). We found that the average amplitude of the μ EPSCs to the second stimulus was greater than that of the first when the first stimulus also evoked a μ EPSC (Supplementary Figures 1D, E, left panels), consistent with paired-pulse facilitation of transmitter release. Moreover, the average amplitude of the μ EPSCs to the second stimulus that followed a failure of response to the first stimulus was identical to, if not greater than, the average of the responses to the second stimulus that followed first stimulus non-failures (Supplementary Figures 1D, E, right panels). These findings are not consistent with failure of the first stimulus to generate an action potential, in which case the amplitude of the μ EPSC to the second stimulus would have been predicted to be the same as that of the first stimulus non-failures. Rather, our findings show that despite the failure of post-synaptic response to the first stimulus an action potential must have been triggered in the axon connected to the lamina I neuron, and must have reached the presynaptic terminal to enhance quantal release of glutamate presynaptically in response to the second stimulus. Therefore, we conclude that the minimal stimulation technique used here reliably evoked a monosynaptic, excitatory post-synaptic response from a single primary afferent connected to each lamina I neuron studied.

When initially searching for a unitary synaptic input in μ EPSC recordings we held the membrane potential at -65 mV ($n = 172$ cells). In all of these recordings when the membrane potential was subsequently held at $+60$ mV we observed a component of the decay phase that was slower than that when the neuron was

held at -65 mV, which we interpret as indicating that there were both AMPAR- and NMDAR-components to the μ EPSCs. In the remainder of recordings we searched with the membrane potential held at $+60$ mV to look for NMDAR-only synapses. However, in all cases we found a rapid inward current when the neuron was subsequently held at -65 mV. Thus, we conclude that all single, primary afferent-to-lamina I neuron synapses we recorded contained both AMPAR and NMDAR components.

Three distinct μ EPSC types evoked across individual adult primary afferent-lamina I neuron synapses

Unitary excitatory postsynaptic currents average amplitude and decay were found to be stable within each single synapse recording (Vh: $+60$ mV) throughout the duration of the recording period (e.g., Figures 1B–D, F, G). However, we observed considerable heterogeneity in the μ EPSC decay between single-synapse recordings (Figure 2A). To gain insight into the diversity in μ EPSCs between recordings we performed principal component analysis (PCA) followed by hierarchical clustering (HC). For the PCA we examined several parameters including charge transfer, half-width, decay constant, peak amplitude, rise time, neuronal input resistance, and synaptic failure rate. Dimensionality reduction of the parameters with PCA (Figures 2B, C and Supplementary Figure 2), showed that the first three components capture 76% of the data variability. Based on this, μ EPSC decay, charge transfer and half-width were retained as electrophysiological parameters that significantly contributed to the first three PCA components (Figure 2C) and, therefore, used to build a classification of individual synaptic responses. To determine whether primary afferent-lamina I neuron synapses are comprised of distinct types, we used μ EPSC decay, charge transfer and half-width for the HC (Figure 2D). Gap-statistic analysis of the clustering (Figure 2D inset top right) identified three as the optimal number of clusters to represent the dataset. We labeled these three groups: fast ($n = 80$, 36% of recorded neurons), intermediate ($n = 114$, 51% of recorded neurons), and slow ($n = 30$, 13% of recorded neurons) based on decay time constant of their μ EPSCs (Figure 2E). Individual representative fast, intermediate, and slow μ EPSCs are shown in Supplementary Figure 3. From these representative μ EPSCs, latency, amplitude, and decay can be seen to be stable throughout each recording (Supplementary Figure 4). Mean μ EPSC traces for each of the three unitary synaptic response types determined by clustering are shown in Figures 3A–C. Across these three groups the following electrophysiological parameters were not different: failure rate (fast $56 \pm 2\%$, intermediate $52 \pm 2\%$, and slow $51 \pm 3\%$), cell input resistance (fast 363 ± 32 MOhm, intermediate 334 ± 19 MOhm, and slow 367 ± 34 MOhm) as well as μ EPSC rise time (fast 2.9 ± 0.2 ms, intermediate 3.1 ± 0.2 ms, and slow 3.4 ± 0.3 ms). Therefore, we conclude that primary afferent-lamina I μ EPSCs at the holding potential of $+60$ mV can be classified into three major groups according to decay constant, half-width, and charge transfer (Figure 3D).

Across these three groups, the μ EPSCs at the holding potential of -65 mV did not differ in peak amplitudes (fast -24 ± 1.4 pA, intermediate -26 ± 0.9 pA, and slow -24 ± 1.6 pA; $p > 0.05$) or

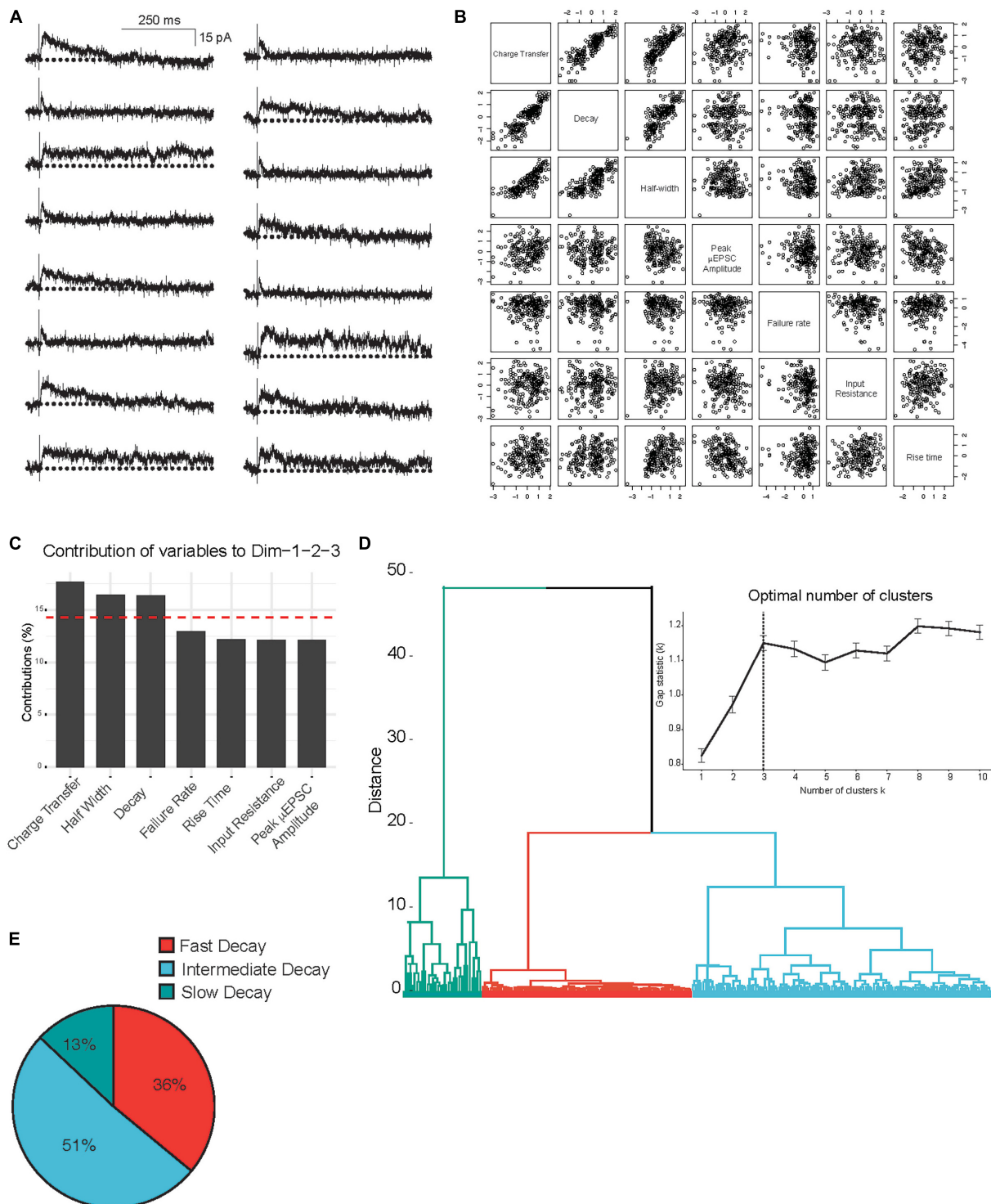


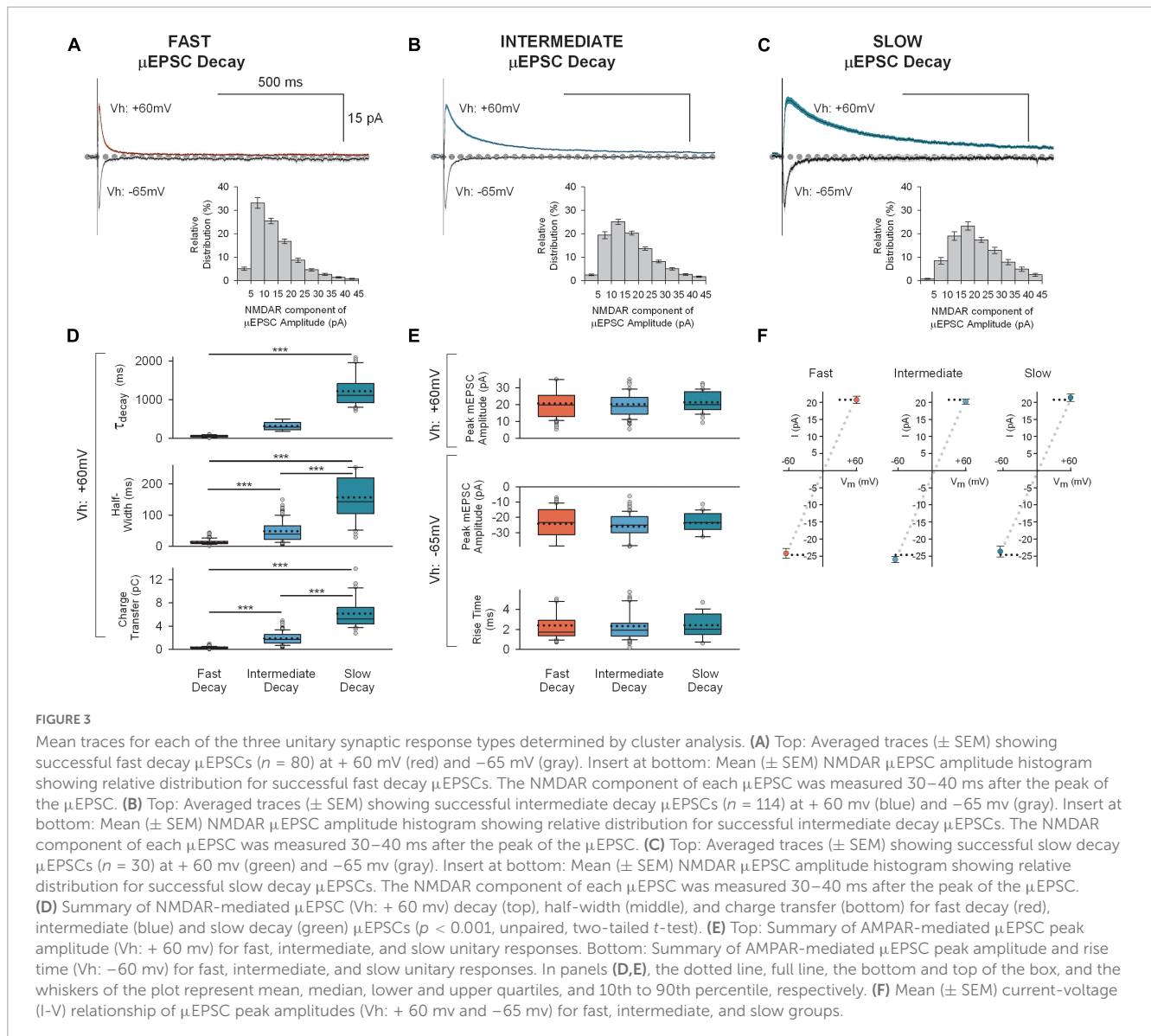
FIGURE 2

Principal component and hierarchical cluster analysis of the electrophysiological parameters of the μ EPSCs recorded (V_h : +60 mV).

(A) Representative μ EPSCs recorded at +60 mV illustrating the diversity of the kinetic properties. (B) Correlation plots of the variables in this study incorporated in the PCA analysis of the 224 independent recordings. (C) Histogram representing the contribution of variables to the three first dimensions, representing 76% of the data variance. The red dashed line on the graph indicates the expected average contribution if the contribution of the variables were uniform. (D) Hierarchical clustering and gap-statistic analysis (inset) of the three first components identify three clusters of responses. (E) The pie chart shows relative (percent) prevalence of distinct μ EPSC types in the full dataset.

in rise times (fast 2.4 ± 0.2 ms, intermediate 2.3 ± 0.2 ms, and slow 2.4 ± 0.3 ms; $p > 0.05$; **Figures 3A–C** below; **Figure 3E**). Moreover, the peak amplitudes of μ EPSCs held at -65 mV

exhibited linear current-voltage relationships (**Figure 3F**). Thus, the AMPAR components of the μ EPSCs were indistinguishable across the three groups.



Distinct GluN2 subtypes mediate the decay kinetics of the three distinct unitary synaptic responses

As the NMDAR component but not the AMPAR component of the μ EPSCs fell into three groups we investigated the basis for the differences in the NMDAR component. Of the three kinetic parameters that account for variance within the population of μ EPSCs, half-width and charge transfer (calculated as area under the curve) occur as a passive function of the time course of the μ EPSC decay (Figure 3). Thus, we inferred from the readily discernible correlation of charge transfer and half-width with decay that the most critical parameter governing the functional importance of each unitary response is time course of the decay itself. We therefore focused our attention on elucidating the mechanism(s) responsible for different μ EPSC decay kinetics. Notably, given that the three distinct μ EPSC decay constants determined from our cluster analysis (52 ± 3 ms for “fast” decay;

315 ± 11 ms for “intermediate” decay; $1,219 \pm 69$ ms for “slow” decay at Vh: +60 mV; $p < 0.001$; Figure 3D) correspond well with values from known NMDAR GluN2 subtypes including specifically GluN1/2A/2A, 2B/2B, and 2D/2D, respectively (Cull-Candy and Leszkiewicz, 2004; Hildebrand et al., 2014), we hypothesized that the dissimilar, yet D-APV-sensitive (Supplementary Figure 5), decay components of unitary synaptic responses represent distinct deactivation kinetics governed by differences in intrinsic properties of distinct GluN2 subtype-containing NMDARs at these synapses.

To test this hypothesis, we rigorously investigated the pharmacological sensitivity of the three distinct response types to known selective NMDAR GluN2 subtype inhibitors. We tested first involvement of GluN2D/2D-containing NMDARs. In a subset of voltage-clamp recordings examining representative “fast,” “intermediate,” and “slow” μ EPSC responses (Vh: +60 mV), we administered to aCSF the GluN2D/2D selective antagonist, DQP-1105 (10 μ M), which is selective for GluN2D/2D diheteromeric NMDARs (Acker et al., 2011) which we refer to here as GluN2D. Fast and intermediate unitary responses were not affected by

DQP-1105 administration (**Supplementary Figures 6B–D, F, G**), whereas the duration of “slow” unitary kinetic responses was reduced by DQP-1105 (**Supplementary Figures 6A, D, E**). Charge transfer of the NMDAR component measured with DQP-1105 present in aCSF was reduced significantly compared to charge transfer during baseline μ EPSC responses before DQP-1105 administration ($p < 0.05$; **Supplementary Figures 6D, E**). Taken together, these results indicate that the particularly prolonged decay of the “slow” μ EPSC response was mediated by GluN2D-containing NMDARs.

We investigated next possible involvement of GluN2B/2B-containing NMDARs by bath administering the GluN2B/2B selective antagonist, Ro25-6981 (1 μ M) which is selective for GluN2B/2B diheteromeric NMDARs (Fischer et al., 1997) which we refer to here as GluN2B. Ro25-6981 was without effect on “fast” decay μ EPSC responses (**Supplementary Figures 7C, D, G**) whereas the duration of the NMDAR component of “intermediate” decay μ EPSC responses was reduced; the NMDAR charge transfer with Ro25-6981 present was decreased significantly ($p < 0.01$) compared to charge transfer during baseline μ EPSC responses prior to Ro25-6981 administration (**Supplementary Figures 7B, D, F**). For “slow” decay responses the intermediate portion of the NMDAR component was affected only moderately by Ro25-6981 while the late NMDAR component of the μ EPSC decay was unaffected (**Supplementary Figure 7A**); charge transfer of the NMDAR component was reduced by Ro25-6981 compared to baseline μ EPSC responses ($p < 0.001$; **Supplementary Figure 7D, E**). We therefore conclude that both “intermediate” and “slow” synapse types are comprised, at least in part, of GluN2B-containing NMDARs.

Having shown that the NMDAR component of “fast” μ EPSC responses was resistant to both Ro25-6981 and DQP-1105 (**Supplementary Figures 6, 7**), we reasoned that “fast” unitary primary afferent-lamina I synaptic responses are mediated by NMDARs other than GluN2B- or GluN2D-containing subtypes. We considered, therefore, the possibility that GluN2A/2A-containing diheteromeric NMDARs which are known to exhibit decay kinetics faster than those of the other GluN2 subunits (Hildebrand et al., 2014) may underlie this NMDAR-mediated synaptic response. To investigate potential function of GluN2A/2A-containing NMDARs (which we refer to here as GluN2A) at these synapses we administered the selective antagonist, TCN-201 (3 μ M) (Hansen et al., 2012). We tested TCN-201 on representative “fast” decay μ EPSC responses and found that the μ EPSC duration was reduced (**Supplementary Figures 8A–C**) to the extent that the entire charge transfer mediated by NMDAR function was abolished ($p < 0.01$; **Supplementary Figures 8D, E**). We conclude that GluN2A-containing NMDARs comprise the “fast” synapse type.

The depressive effect of Ro25-6981 on slow decay μ EPSCs (**Supplementary Figures 7A, D, E**) suggests function of GluN2B-containing in addition to GluN2D-containing NMDARs at “slow” decay synapses. In addition, that the residual “DQP-1105-insensitive” NMDAR component of “slow” decay μ EPSCs showing sensitivity to DQP-1105 is comparable to “intermediate” μ EPSC responses (**Supplementary Figures 6A, D–F**) further provides evidence for GluN2B subtype NMDARs in addition to GluN2D-containing NMDARs at “slow” decay synapses. Furthermore, though we did not examine specifically TCN-201 on “intermediate” and “slow” decay μ EPSC responses, we are not ruling out a

contribution of GluN2A-containing NMDAR function at these synapses. For example, the $\tau_{(fast)}$ for “intermediate” decay μ EPSCs (45 ± 4 ms) is comparable ($p > 0.05$) to the τ value for “fast” (GluN2A-mediated) μ EPSC decay kinetics (52 ± 3 ms; **Figure 3D**). It is also evident from “intermediate” decay μ EPSCs which showed sensitivity to Ro25-6981 that the remaining “Ro25-6981-insensitive” NMDAR component is comparable to the “fast” decay μ EPSC responses (**Supplementary Figures 7C, D, F, G**). Based on these observations, we are not excluding the possibility that “intermediate” and possibly “slow” synapses may also contain GluN2A-containing NMDARs.

Differential Mg^{2+} block of fast, intermediate, and slow μ EPSCs

GluN2 subunit differences in the kinetics of Mg^{2+} unblock contribute to NMDAR subtype function in current flow during membrane depolarization at glutamatergic synapses (Clarke and Johnson, 2006). Given the distinct GluN2 kinetic properties determined from the three μ EPSC types recorded at the holding potential of +60 mV (**Figures 3A–D**), we reasoned that μ EPSCs recorded from the same experiments but at the negative holding potential of –65 mV (**Figures 3A–C** bottom) would also reflect differences in biophysical properties indicative of distinct GluN2 subtypes. Consistent with this prediction, the late component of negatively held μ EPSCs exhibited significant differences in half-width ($p < 0.01$) and charge transfer ($p < 0.05, 0.01, 0.001$) across the three groups (**Supplementary Figure 9A**) that may be attributed to differences in sensitivity of GluN2 subtypes to Mg^{2+} block (Kuner and Schoepfer, 1996; Clarke and Johnson, 2006). By determining the Mg^{2+} -induced percent inhibition of the amplitude of the NMDAR component of μ EPSCs recorded at the holding potential of –65 mV in each group (**Supplementary Figure 9B**) we found that the inhibition of the NMDAR component of μ EPSCs from the “fast” cluster was similar to that of μ EPSCs from the “intermediate” cluster, whereas the Mg^{2+} -induced percent inhibition of the NMDAR component of μ EPSCs from the “slow” cluster was substantially less (**Supplementary Figure 9B**; Kuner and Schoepfer, 1996; Clarke and Johnson, 2006). We conclude that the differences in Mg^{2+} block of μ EPSC NMDAR components at primary afferent-lamina I glutamatergic synapses further confirm the distinctiveness of GluN2-containing NMDAR subtype expression and function we propose to occur at these synapses.

No evidence for presynaptic NMDAR function

We reasoned that if NMDARs functioned presynaptically to influence synaptic transmission, we would observe a change in unitary synaptic failure rate. We found that failure rate remained stable in recordings in which D-APV, TCN-201, Ro25-6981, or DQP-1105 was tested (**Supplementary Figures 10A–C**). In a representative experiment, D-APV is shown to inhibit the NMDAR component of the μ EPSC (mean \pm SEM) while exhibiting no effect on failure rate (**Supplementary Figure 10A**) consistent with

a postsynaptic function of NMDARs at primary afferent-lamina I neuron synapses.

μ EPSP temporal summation at individual synapses is NMDAR-dependent

The diversity of GluN2-containing NMDARs at individual lamina I synapses and their differences in Mg^{2+} block prompted us to investigate next the function of GluN2 subtype diversity at individual primary afferent-lamina I neuron synapses. We carried out minimal stimulation in voltage-clamp first to establish *bona fide* μ EPSC responses (Vh: -65 mV) after which, within the same recording, we switched to current-clamp mode to monitor membrane potential (μ EPSP response using a K^+ -based intracellular solution). In this dual mode recording protocol we used a brief train composed of 5 stimuli delivered every 200 ms [5 Hz frequency which mimics low repetitive firing pattern of nociceptors (Matsumoto et al., 2006)] at 5 s intervals (0.2 Hz) in voltage clamp (Supplementary Figures 11A, B) and then current clamp (Supplementary Figures 11C, D) modes for a given lamina I recording.

Continuous sweep recordings of μ EPSCs during the 5 Hz minimal stimulus train show that mean (\pm SEM) peak amplitude, half-width, and rise time remained stable ($p > 0.05$; Supplementary Figures 11A, B). Though an increase in μ EPSC mean (\pm SEM) charge transfer was observed over successive stimuli ($p < 0.01$), pure μ EPSC responses (without failures) at each stimulus throughout the 5 Hz train remained stable; peak amplitude, charge transfer, half-width, and rise time for the five μ EPSCs in the 5 Hz train were not significantly different ($p > 0.05$; Supplementary Figures 12A, B). A decrease in failure rate was found between the first and fifth pure μ EPSCs (successes only) in the 5 Hz train ($p < 0.05$; Supplementary Figure 12B). Though indicative of increased presynaptic glutamate release probability through the progression of the 5 Hz train, we do not consider this to have influenced postsynaptic mechanisms during the train because each pure μ EPSC response (without failures) remained constant.

Continuous sweeps recorded in current clamp mode during the 5 Hz train showed that membrane potential depolarized progressively with each stimulus, peaking after the fifth stimulus, a response we refer to as a “ μ EPSP burst” (Supplementary Figures 11C, D). Pure μ EPSP responses (successes only) shown at each stimulus (mean \pm SEM) during the 5 Hz train exhibited a progressive increase in peak amplitude, area, half-width, decay, and prestimulus membrane potential ($p < 0.001$; Supplementary Figures 13A, B), while rise time across the five μ EPSPs in the train was not different ($p > 0.05$; Supplementary Figures 13A, B). Notably, the failure rates for the first and fifth μ EPSPs were indistinguishable from those for the corresponding first and fifth μ EPSCs recorded in voltage clamp ($p > 0.05$; Supplementary Figure 12B) which indicate that the transition in recording mode (from voltage clamp) was inconsequential to mechanisms underlying unitary synaptic transmission as we were able to evoke reliable μ EPSPs that summate with a failure rate that was indiscernible from that during μ EPSC recordings.

In a representative example μ EPSP burst, D-APV was without effect on the rising phase or the peak amplitude of the first μ EPSP

in the 5 Hz train but reduced μ EPSP decay and abolished temporal summation (Supplementary Figure 14A). Similarly, the NMDAR channel blocker, MK-801, reversed the summated component of the μ EPSP burst (Supplementary Figure 14B). Taken together, we conclude that temporally patterned μ EPSPs evoked during the 5 Hz stimulus train exhibit summation and that μ EPSP decay and summation are dependent on NMDAR function.

Distinct μ EPSP kinetics across individual primary afferent-lamina I neuron synapses

Having determined that that temporal summation of μ EPSPs at this synapse is attributable to NMDAR function (Supplementary Figure 14), we reasoned that GluN2 subtype synaptic distinctiveness (Figures 2, 3 and Supplementary Figures 2–9) may underlie possible heterogeneity in our μ EPSP burst dataset. In one approach to elucidate potential diversity in μ EPSP burst properties, we grouped μ EPSP bursts based on lamina I neuron type (Figures 4A–C). In each current-clamp recording, in which we had acquired also membrane potential in response to depolarizing current injection (20 pA for 1 s), we identified in lamina I neurons distinct firing properties in response to current injection. This enabled us a subclassification of our μ EPSP dataset based on neuron spiking properties including single/non-spiking, delayed/phasic spiking, or tonic spiking activity (Figures 4A–C), established features of lamina I neurons (Yasaka et al., 2010; Punnakkal et al., 2014; Browne et al., 2020). We examined kinetic properties from the first μ EPSP in the burst as it was the μ EPSP in the stimulus train without summation, and from the last (fifth) μ EPSP in the burst as it exhibited the greatest degree of summation (Supplementary Figure 13). Within lamina I neuron type, pure μ EPSPs (successes only, mean \pm SEM) exhibited an increase in area, half-width, decay, and prestimulus membrane potential of the fifth μ EPSP vs. the first μ EPSP ($p < 0.05$, $p < 0.01$, $p < 0.001$, Figures 4E–H). Between lamina I neuron type, pure first and fifth μ EPSPs exhibited differences in area, half-width, and decay ($p < 0.05$, $p < 0.01$, $p < 0.001$; Figures 4E–G). Pure fifth μ EPSPs between neuron type also exhibited significant differences in peak amplitude and prestimulus membrane potential ($p < 0.05$, $p < 0.01$, $p < 0.001$; Figures 4D, H). These results show that primary afferent-lamina I neuron synapses possess distinct kinetic properties that enable μ EPSP temporal summation capability (Figures 4D–H). Importantly, μ EPSP summation capacity at a given primary afferent synapse shows correlation with lamina I neuron type (single/non-spiking < delayed/phasic spiking < tonic spiking).

In another approach to elucidate potential μ EPSP diversity we applied unsupervised HC analysis to the μ EPSP burst dataset. μ EPSP kinetic properties including pure first and fifth μ EPSP half-width, area, and decay were used for HC which identified three distinct clusters (Figures 5A–C) referred to as “fast,” “intermediate” and “slow” kinetic properties which we compared to μ EPSP classification based on lamina I neuron type (Figure 5D). Clusters representing first and fifth μ EPSP responses from tonic spiking neurons (Figure 5D) corresponded entirely with clusters representing “slow” μ EPSP kinetics for both the first and fifth

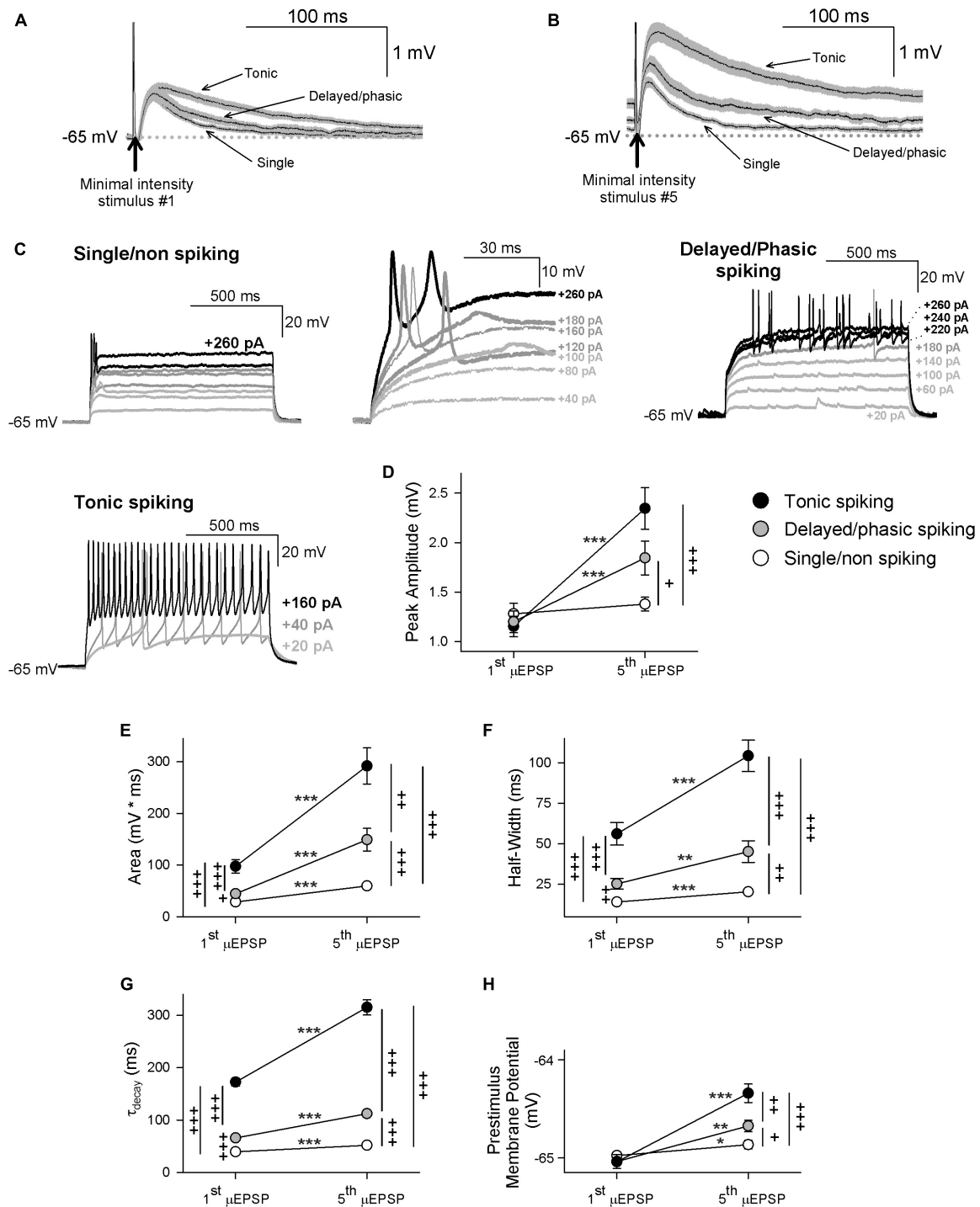
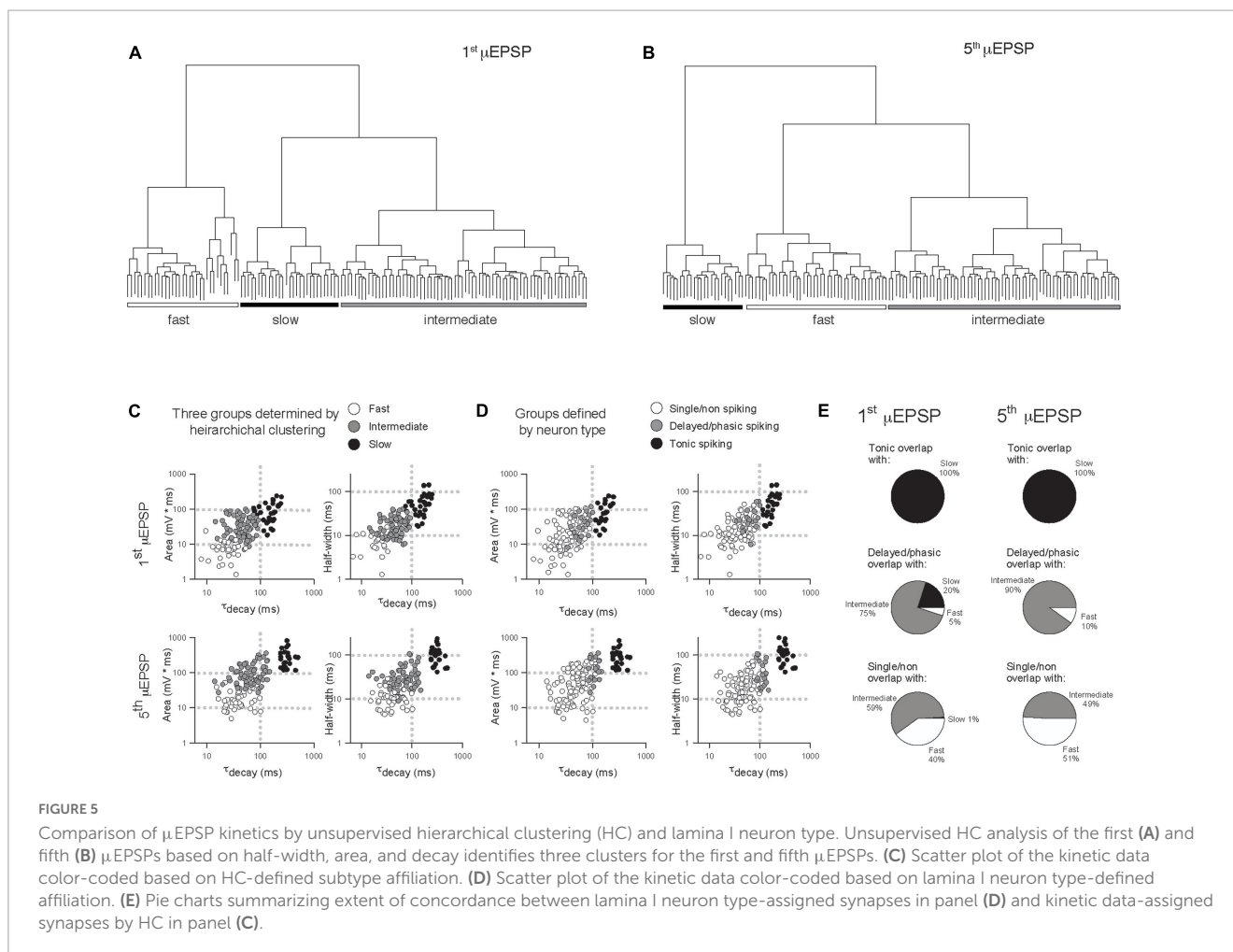


FIGURE 4

First and fifth μ EPSP responses recorded from single/non-spiking, delayed/phasic spiking, and tonic spiking lamina I neuron types. (A) Pure mean (\pm SEM) μ EPSP traces (without synaptic failures) shown for the first (A) and fifth (B) minimal stimulus during the 5 Hz train (arrows indicate stimulus artifacts) for single/non-spiking, delayed/phasic spiking, and tonic spiking lamina I neurons. (C) Representative responses to current injection (20 pA for 1s) of each lamina I neuron type including single/non-spiking (inset at right shows magnified view), delayed/phasic spiking, and tonic spiking. (D) Scatter plots (mean \pm SEM) showing μ EPSP peak amplitude for the first and fifth μ EPSPs from tonic spiking (black symbol), delayed/phasic spiking (gray symbol), and single/non-spiking (white symbol) lamina I neurons (μ EPSP #1 vs. #5, * $p < 0.05$, ** $p < 0.01$, or *** $p < 0.001$, paired t -test; + $p < 0.05$, + + $p < 0.01$, or + + + $p < 0.001$ between lamina I spiking types at μ EPSP #1 and #5, t -test), (E) area, (F) half-width, (G) decay, and (H) prestimulus membrane potential.

μ EPSP responses (Figures 5C–E, black symbols) indicative of a homogenous distribution of primary afferent synapses with “slow” μ EPSP kinetic properties occurring on tonic spiking lamina I

neurons (Figure 5E). Clusters representing delayed/phasic spiking neurons (Figure 5D, gray symbols) were affiliated predominantly with “intermediate” clusters for the first and fifth μ EPSPs



(Figures 5C–E) while a small portion of μ EPSP responses were affiliated with either “fast” (Figures 5C, E) or “slow” (Figures 5C, E) clusters. Clusters representing single/non-spiking neurons for the first and fifth μ EPSPs (Figure 5D, white symbols) overlapped with both “fast” and “intermediate” kinetics (Figures 5C–E, white and gray symbols) but not with “slow” kinetics (Figures 5C–E, black symbols). We conclude that first and fifth μ EPSPs can be classified into three major groups consisting of “fast,” “intermediate,” or “slow” kinetics according to half-width, area, and decay (Figures 5A–C). Notably, single/non-spiking lamina I neurons contain primary afferent synapses with predominantly “fast” and “intermediate” postsynaptic kinetic properties, while delayed/phasic spiking neurons contain primary afferent synapses with predominantly “intermediate” postsynaptic properties and some with “fast” kinetic properties. Tonic spiking neurons contain primary afferent synapses with exclusively “slow” postsynaptic kinetic properties.

Link between lamina I neuron type and μ EPSP summation capacity is GluN2 subtype-dependent

Having determined that primary afferent-lamina I neuron synapses contain distinct NMDAR GluN2-containing subtypes

(Figures 2–3 and Supplementary Figures 2–9), that temporal summation of μ EPSPs at these synapses is attributable to NMDAR function (Supplementary Figure 14), and that HC identified three distinct μ EPSP burst clusters, we reasoned that intrinsic properties of μ EPSP burst summation capacity derive from distinct primary afferent-lamina I neuron postsynaptic GluN2 subtype-containing NMDARs. To elucidate the role of GluN2 subtype in μ EPSP temporal summation, we therefore probed the pharmacological sensitivity of primary afferent-evoked μ EPSP bursts recorded from lamina I neurons with known spiking patterns using the selective inhibitor for GluN2A (TCN-201; 3 μ M), GluN2B (Ro25-6981; 1 μ M), or GluN2D (DQP-1105; 10 μ M) administered to aCSF. Baseline μ EPSP burst area (mean \pm SEM) determined from single/non-spiking (88 ± 16 mv^*ms), delayed/phasic spiking (115 ± 20 mv^*ms), and tonic spiking (295 mv^*ms) neurons (Figures 6D, H, K, respectively) exhibited a progressive increase across neuron type consistent with neuron type-specific temporal summation in our dataset (Figure 4E). TCN-201 inhibited μ EPSP burst responses from single/non- (Figures 6A, D; $n = 4$) and delayed/phasic spiking lamina I neuron (Figures 6E, H; $n = 1$) but was without effect on a μ EPSP burst recorded from a tonic spiking lamina I neuron (Figures 6I, K; $n = 1$). Ro25-6981 was also found to inhibit μ EPSP burst responses from single/non-spiking (Figures 6C, D; $n = 1$) and delayed/phasic spiking (Figures 6E, H; $n = 4$) lamina I neurons. However, in experiments

in which we tested involvement of GluN2D-containing NMDARs, DQP-1105 was without effect on μ EPSP bursts recorded from single/non-spiking (Figures 6B, D; $n = 1$) and delayed/phasic spiking (Figures 6G, H; $n = 3$) lamina I neuron types but inhibited the μ EPSP burst recorded from a tonic spiking lamina I neuron (Figures 6J, K; $n = 1$). Our results identify GluN2A and 2B subtype function at primary afferent synapses on single/non-spiking and delayed/phasic spiking lamina I neurons while the GluN2D NMDAR subtype functions predominantly at primary afferent synapses on tonic spiking lamina I neurons. Taken together, we conclude that GluN2 subtypes occur with diversity across different lamina I neuron types and that μ EPSP summation at the level of individual primary afferent-lamina I neuron synapses is dependent on distinct GluN2 subtype(s) composition and function at the synapse.

Discussion

Our strategy to examine single synapse fidelity postsynaptic responses to evoked primary afferent input in the adult rat spinal lamina I subfield identifies this sensory synapse as a major locus of diversity that arises from a heterogeneous postsynaptic compartmentalization of single or multiple distinct GluN2 subtypes. We show further that the distinct postsynaptic GluN2 subtype(s) configuration at a given individual afferent synapse on a lamina I neuron defines precisely the computational capability and strength of that synapse.

Single or multiple GluN2 subtype configurations at primary afferent-lamina I neuron synapses

Principal component and hierarchical analysis combined with GluN2 pharmacological testing of μ EPSCs recorded from hundreds of individual primary afferent-lamina I neuron synapses identified distinct postsynaptic GluN2 subtype configurations. To our knowledge this is the first demonstration of higher-order assembly of distinct GluN2 subtypes of the NMDAR occurring either individually or in defined combinations at a fully developed, mammalian, principal sensory glutamatergic synapse. Super-resolution imaging in cultured hippocampal neurons has described precise control of the spatial organization of distinct GluN2 subtypes (GluN2A and 2B to date) in defined postsynaptic nanodomains in the PSD by specific PSD protein constituents (Kellermayer et al., 2018; Hruska et al., 2022). In the present study, minimal stimulation in our *ex vivo* slice preparation enabled us to evoke glutamate release at single synapse resolution and therefore identify at individual synapses functionally relevant postsynaptic GluN2 localization(s) which we found to consist of GluN2A alone, GluN2A and 2B, or GluN2B and 2D. We consider these findings as conclusive evidence of functionally distinct postsynaptic GluN2 subtype organization at individual mammalian glutamatergic synapses.

Previous investigations documenting GluN2 subtype content in spinal lamina I and II have used high intensity stimulation-evoked EPSCs (Tong et al., 2008; Shiokawa et al., 2010;

Tong and MacDermott, 2014) or spontaneously occurring mEPSCs (Hildebrand et al., 2014) from populations of synapses. Although these studies provide insight into GluN2 subtype content in the superficial dorsal horn, stimulus protocols that elicit activation of a synapse population are not amenable to elucidating single or multiple GluN2 subtype configurations and function at an individual primary afferent-lamina I neuron synapse. Furthermore, recording miniature or spontaneous unitary synaptic events do not resolve responses in a population of synaptic inputs from responses of an individual synapse. The single-synapse fidelity of our recordings here enabled us to acquire and study defined unitary synaptic events at individual primary afferent-lamina I neuron monosynaptic connections and investigate at high resolution GluN2 subtype diversity and function.

Functional implications of GluN2 subtype on synaptic computation and transmission in spinal lamina I

Voltage-dependent inward currents mediated by sodium and calcium channels have been proposed to modulate EPSP pattern and integration in the brain (González-Burgos and Barrionuevo, 2001) and spinal cord dorsal horn (Prescott and De Koninck, 2005). The differences in Mg^{2+} block of the distinct μ EPSC NMDAR components found here at individual primary afferent-lamina I neuron glutamatergic synapses (Supplementary Figure 9) not only substantiate the postsynaptic organization of GluN2A, GluN2A and 2B, or GluN2B and 2D we propose to occur at these synapses but highlight their distinct biophysical properties with implications in current flow through NMDARs during membrane depolarization (Kuner and Schoepfer, 1996; Clarke and Johnson, 2006). We show here that evoked unitary depolarizations at primary afferent-lamina I neuron monosynaptic connections are dependent on both AMPAR- and NMDARs. Our findings further indicate that μ EPSP decay and summation throughout the μ EPSP burst is shaped primarily by NMDAR-mediated current (Figure 6 and Supplementary Figure 14) opening the possibility that NMDARs also contribute to the integrative kinetics underlying subthreshold synaptic membrane depolarization (Pitcher et al., 2011).

In addition to acquiring evoked μ EPSP bursts, current injection in our recordings elucidated spiking characteristics of lamina I neurons including single/non-spiking, delayed/phasic spiking, or tonic spiking (Yasaka et al., 2010; Punnakkal et al., 2014; Browne et al., 2020). This enabled us to classify μ EPSP burst properties by neuron spiking type (Figure 4). However, a definitive correlation could not be made with the three μ EPSP clusters categorized by lamina I neuron spiking type and the three clusters of μ EPSP kinetics determined by HC analysis (Figures 5C-E). Though μ EPSPs clustered by the tonic spiking lamina I neuron type corresponded entirely with the slower and more prolonged μ EPSPs classified by HC analysis, this was not the case for the other two neuron types. Delayed/phasic spiking lamina I neurons exhibited μ EPSP kinetic properties that corresponded predominantly with those of intermediate μ EPSP kinetics classified by HC while a small percentage of μ EPSPs exhibited kinetic properties consistent with fast and slow kinetics defined by HC. Furthermore, μ EPSPs evoked

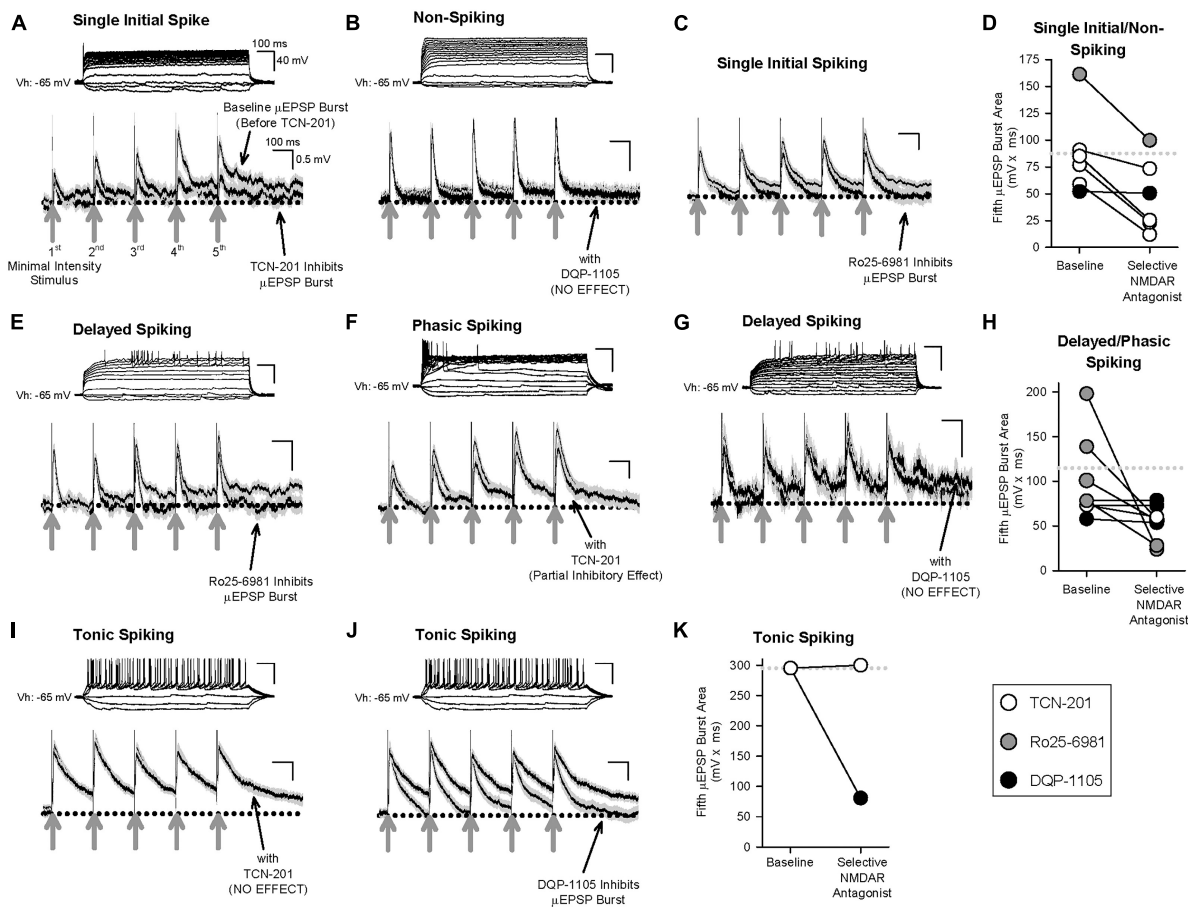


FIGURE 6

Effect of selective inhibitors for GluN2A (TCN-201), GluN2B (Ro25-6981), or GluN2D (DQP-1105) on representative μ EPSP bursts recorded from the three lamina I neuron types. Given the continuous nature of these recordings, μ EPSP burst traces include both successes and failures. (A–D) μ EPSP bursts recorded from single/non-spiking lamina I neurons showing sensitivity to TCN-201 (A) and Ro25-6981 (C), but not to DQP-1105 (B). (D) Summary scatter plot showing fifth μ EPSP burst area at baseline and during administration of the selective GluN2 inhibitor to aCSF. (E–H) μ EPSP bursts recorded from delayed/phasic spiking lamina I neurons showing sensitivity to Ro25-6981 (E) and TCN-201 (F), but not to DQP-1105 (G). (H) Summary scatter plot showing fifth μ EPSP burst area at baseline and during administration of the selective GluN2 inhibitor to aCSF. (I–K) μ EPSP bursts recorded from a tonic spiking lamina I neuron did not exhibit sensitivity to TCN-201 (I) but exhibited sensitivity to DQP-1105 (J). (K) Summary scatter plot showing fifth μ EPSP burst area at baseline and during administration of the selective GluN2 inhibitor to aCSF. In panels (D,H,K), the dotted line in the plot represents the mean of the baseline of the fifth μ EPSP burst area. Action potential traces shown above each μ EPSP burst are representative of that μ EPSP burst recording.

at single/non-spiking lamina I neurons exhibited kinetic properties that corresponded almost equally with fast and intermediate μ EPSP kinetic properties determined by HC. The overall concept that emerges from these results is that μ EPSP classification is not exclusively neuron specific but rather synapse specific in that μ EPSP kinetics in a given HC-defined group can be found in different lamina I neuron types. μ EPSP kinetic properties that are either identical for a given neuron type, i.e., neuron-specific, or distinctly different within a given neuron type, i.e., synapse-specific, exemplify diversity in the individual μ EPSP itself as well as temporal summation capability at primary afferent-lamina I neuron synapses that have major functional implications in subthreshold synaptic computation and strength for lamina I neurons to temporally patterned sensory input. No other study that we are aware of has demonstrated this degree of heterogeneity in primary afferent-evoked μ EPSP responses at individual synapses within and between distinct lamina I neuron types.

The three μ EPSP clusters we report here are unexpected because they do not correspond to unitary synaptic depolarization kinetics reported previously in the spinal dorsal horn (Prescott and De Koninck, 2005). Prescott and De Koninck (2005) found that subthreshold depolarization measured from spontaneous EPSPs (sEPSPs) was similar to that from both delayed/phasic and single spiking lamina I neurons while sEPSPs from tonically spiking lamina I neurons exhibited markedly prolonged depolarization kinetics (Prescott and De Koninck, 2005), consistent with two classifications of unitary sEPSP kinetics. We do not have a clear explanation for this apparent discrepancy, but the possibility can't be excluded that the spontaneous events in the study by Prescott and De Koninck (2005) may have derived from synaptic inputs other than primary afferents. We therefore consider the prospect that mechanisms underlying the kinetics of unitary depolarizations at the primary afferent-lamina I synaptic connection may be distinctly different from those at non-primary afferent synaptic connections. In addition, the number

of unitary synaptic recordings obtained in the present study also merit consideration in that they are relatively high and may therefore favor increased opportunity to detect and decipher previously unrecognized synaptic distinctiveness of NMDAR-dependent biophysical properties of evoked μ EPSPs at the primary afferent-lamina I neuron synapse.

The three μ EPSC and three μ EPSP clusters identified by HC analysis (Figures 2, 5, respectively) support the idea that three distinct GluN2-dependent mechanisms may be at play in mediating different stimulus-evoked membrane depolarization at individual primary afferent-lamina I neuron synapses. The selective GluN2D inhibitor, DQP-1105, was found to be without effect on fast and intermediate μ EPSP decay and burst responses in recordings from single/non-spiking and delayed/phasic lamina I neurons (Figures 6B, D, G, H), but depressed the μ EPSP burst exhibiting slow decay kinetics and robust temporal summation recorded from a tonic spiking neuron (Figures 6J, K). Thus, GluN2D subtype-dependent slow kinetic properties therefore function to broaden μ EPSP decay and integrative capacity, and ultimately facilitate burst summation capability to temporally patterned afferent synaptic input to tonic spiking lamina I neurons. The selective GluN2A inhibitor, TCN-201, was without effect on slow μ EPSP decay and summation in a recording from a tonic spiking lamina I neuron (Figures 6I, K), but depressed μ EPSP bursts exhibiting fast decay kinetics and low temporal summation in recordings from single/non- and delayed/phasic spiking neurons (Figures 6A, D, F, H). GluN2A subtype-dependent fast kinetic properties therefore function to accelerate μ EPSP decay and limit integrative capacity to temporally patterned afferent synaptic input. The selective GluN2B inhibitor, Ro25-6981, depressed μ EPSP bursts displaying intermediate kinetic properties in recordings from single/non- and delayed/phasic spiking lamina I neurons (Figures 6C–E, H) indicative of GluN2B subtype-dependent function in mediating intermediate μ EPSP decay and temporal summation. The main concept that emerges from our data is that decay and summation capacity of μ EPSPs evoked at a given primary afferent-lamina I neuron synapse are functionally dependent and shaped by the distinct GluN2 subtype synaptic predominance at that synapse which signals to narrowly, intermediately, or widely tune, respectively, the duration of evoked unitary depolarization from resting membrane potential. Ultimately, this would have major implications in subthreshold integrative capacity of different lamina I neuron types to temporally patterned glutamatergic input from an ensemble of primary afferents.

The effects of the selective GluN2 subtype inhibitors examined in our μ EPSC recordings revealed that the GluN2 subtype with the longest decay at a given synapse is the main identifiable GluN2 subtype responsible for carrying the greatest charge transfer at that synapse (Supplementary Figures 6, 7). Implicit to these results is that the GluN2 subtype(s) exhibiting residual kinetics identifies multiple possible GluN2 subtype combinations localized at a synapse. Taking into account the GluN2A, 2A and 2B, and 2B and 2D synaptic configurations determined in our voltage clamp experiments, we therefore propose the scenario in which primary afferent synaptic connections to single/non-spiking lamina I neurons may contain GluN2A only or GluN2A and 2B postsynaptically, while primary afferent synaptic connections to delayed/phasic neurons may contain postsynaptically GluN2A and

2B and some GluN2A only. Primary afferent synapses on tonic spiking lamina I neurons appear to be comprised exclusively of GluN2B and 2D postsynaptically. Although these data together provide evidence to suggest postsynaptic localization of distinct single or multiple GluN2 subtypes at individual synapses on specific lamina I neuron types, it is unclear the functional necessity or significance of multiple distinct GluN2 subtypes exhibiting differing kinetic properties at a given synapse. We reason that multiple postsynaptic GluN2 subtype configurations may endow primary afferent-lamina I neuron synapses with a more diverse GluN2 subtype-dependent modulation of membrane potential (and possibly other forms of GluN2 subtype-dependent signaling) that imparts stringent control of transmission efficacy.

Single cell transcriptional analysis of neurons in the rodent spinal dorsal horn (Häring et al., 2018) has identified 15 inhibitory (GABAergic) and 15 excitatory (glutamatergic) molecular subtypes of neuron in which *Grin2b* occurs abundantly in both excitatory and inhibitory subtypes, while *Grin2d* is low in excitatory and moderately expressed in inhibitory neurons, and *Grin2a* is found to be low in inhibitory and low to moderate in excitatory neurons. We did not explicitly attempt here to resolve GluN2 subtype function in inhibitory vs. excitatory lamina I neurons. We did, however, acquire the spiking pattern of the lamina I neurons recorded in current clamp, as described above. Notably, tonic spiking spinal dorsal horn neurons are generally classified as inhibitory (Yasaka et al., 2010; Punnakal et al., 2014), but accumulating evidence shows a proportion of this neuron spiking type to be excitatory (Yasaka et al., 2010; Browne et al., 2020). Furthermore, though delayed/phasic spiking dorsal horn neurons have been shown to be inhibitory (Punnakkal et al., 2014; Browne et al., 2020), they have also been shown to be predominantly excitatory (Yasaka et al., 2010; Punnakal et al., 2014; Browne et al., 2020). Similarly, though a small proportion of single/non-spiking dorsal horn neurons have been found to be inhibitory (Punnakkal et al., 2014; Browne et al., 2020), this neuron type has also been found to be predominantly excitatory (Yasaka et al., 2010; Punnakal et al., 2014; Browne et al., 2020). Notwithstanding these apparent discrepancies, the synapse-specificity we propose here, rooted in distinct GluN2 subtype configurations and computation capability, may represent a basis on which multiple CNS mechanisms (e.g., excitatory and inhibitory) are driven by glutamatergic synaptic input and tightly modulated by distinct postsynaptic GluN2 subtype configurations.

Synaptic GluN2 subtype heterogeneity as a determinant of transmission fidelity in the CNS

We used the *ex vivo* primary afferent-lamina I neuron synaptic preparation as a model glutamatergic circuit in which single-synapse fidelity postsynaptic responses were investigated. Based on our results showing synapse-specific GluN2 subtype heterogeneity across individual glutamatergic synapses, we propose for consideration major roles of GluN2 subtype diversity in neuron excitability throughout the CNS. The functional dependence of μ EPSP shape and μ EPSP burst summation capacity on the diverse single or multiple GluN2 subtype configurations with differing kinetics at a given synapse would be predicted, in an ensemble

of glutamatergic inputs, to impact EPSP-spike coupling (Li and Gullidge, 2021) by gauging membrane potential depolarization and, ultimately, the neuron reaching spiking threshold. We also put forward here the concept that GluN2 protein subtype heterogeneity in synaptic ensembles to a given neuron may serve a coding function that coordinates the synaptic integrative fidelity of that neuron to repetitive input activity (coincidence detection) which, importantly, would further influence neuron firing.

The NMDAR dendritic spike is the dominant mechanism by which dendritic integration of glutamatergic inputs through the recruitment of NMDAR channels leads to firing of a neuron (Schiller and Schiller, 2001; Antic et al., 2010). Since its discovery in cortical pyramidal cell dendrites over 20 years ago (Schiller et al., 2000) the NMDAR spike continues to receive considerable focus in different cortical regions (Enoki et al., 2004; Manita et al., 2011; Lavzin et al., 2012; Palmer et al., 2014; Kumar et al., 2018; Otor et al., 2022). Notably, recent evidence has uncovered critical features of NMDAR-containing synapses that contribute to the generation of spikes including synapse number (Plotkin et al., 2011), proximity to other synapses (Plotkin et al., 2011), spatial clustering (Poleg-Polsky, 2015; Weber et al., 2016; Scholl et al., 2021), as well as their dendritic location (Froemke et al., 2010; Menon et al., 2013; Gao et al., 2021). Given our findings here, we propose for consideration the potential role GluN2-dependent synaptic diversity and organization may impose on dendritic spike threshold and efficacy in firing in neurons in which NMDAR spikes predominate.

Key distinctions in structural features of individual glutamatergic synapses including spine size, volume (Matsuzaki et al., 2004; Arellano et al., 2007; Holtmaat and Svoboda, 2009; Bopp et al., 2017; Holler et al., 2021), and PSD area (Konur et al., 2003; Gray et al., 2006; Statman et al., 2014; Kilinc, 2018; Borczyk et al., 2019) show correlation with physiological transmission strength. Whether or not proteomic complexity at synapses including that of GluN2 synaptic heterogeneity may be causative, correlative (Antal et al., 2008; Hruska et al., 2022), or independent of PSD or synapse size (Racca et al., 2000; Shinohara and Hirase, 2009; Hruska et al., 2022), we suggest that synaptic distinctiveness, rooted in GluN2 subtype diversity, is a critical determinant in grading subthreshold glutamatergic synaptic strength.

Molecular and architectural complexity across glutamatergic synapses, arising from a multitude of differences in postsynaptic proteome constituents and their nanostructure organization (Frank and Grant, 2017; Roy et al., 2018a,b), are beginning to emerge as determinants of individual synaptic diversity in the brain (Grant and Fransén, 2020) and spinal dorsal horn (Broadhead et al., 2020). We demonstrate here that a major locus of proteome complexity exists in the spinal lamina I nociceptive subfield and involves extensive postsynaptic GluN2 subtype diversity at the primary afferent-lamina I neuron synapse. Collectively, our data are consistent with a model wherein synapse-specific organization of distinct GluN2 subtypes serves as a fundamental subthreshold coding mechanism and a core determinant of how physiological sensory information is processed and transferred from the periphery to the brain. Future studies that scrutinize NMDAR subtype diversity and function at this principal sensory synapse in models of neuropathy and inflammation will undoubtedly advance our understanding of synaptic mechanisms underlying chronic pain associated with trauma or disease. Our findings also

offer insight into complexity of glutamatergic synapses and their function in other regions of the CNS in health and disease.

Materials and methods

Animals

Experiments were carried out using adult, male Sprague Dawley rats (from Charles River, P70–80, 325–350 g), and approved by the Hospital for Sick Children Animal Care Committee and in accordance with policies of the Canadian Council on Animal Care.

Spinal cord isolation and slice preparation

The lumbar spinal cord was isolated from anesthetized rats (urethane administered by intraperitoneal injection, 20% [(wt/vol)] by rapid dissection through ventral laminectomy and placed immediately in ice-cold protective artificial cerebrospinal fluid (paCSF) solution containing (in mM): 82 NaCl, 3 KCl, 1.25 NaH₂PO₄, 9.3 MgCl₂, 24 D(+)-glucose, 20 NaHCO₃, 0.1 CaCl₂ and 70 sucrose (chemicals from Sigma Millipore) saturated in carbogen (95% O₂, balance 5% CO₂; pH 7.40 and 315–325 mOsm). After removal of the meninges and ventral roots under a dissecting microscope (Leica MS 5), the ventral surface of the lumbar segment was glued (Vetbond, 3 M) to an agar block (4% agarose, low melting point, analytical grade, Promega, Fisher Scientific; 4% agarose was prepared using raCSF [see below]) in a vertical orientation which in turn was glued in place in a vibratome (Leica VT1000 S) slicing chamber containing ice-cold, carbogen-saturated paCSF for slice preparation. Following sectioning (blade advance speed of ~ 0.02–0.03 mm/s and lateral amplitude of ~2.5 mm), transverse spinal cord slices (500–600 μm) containing the dorsal rootlets were transferred to incubation aCSF (iaCSF) containing (in mM): 90 NaCl, 3 KCl, 1.25 NaH₂PO₄, 9.7 MgCl₂, 24 D(+)-glucose, 19 NaHCO₃, 0.1 CaCl₂ and 60 sucrose saturated with carbogen (pH 7.40, 315–325 mOsm) and maintained at 30 ± 1°C until recording.

Electrophysiology and data acquisition

For data acquisition, a single transverse spinal cord slice was transferred to the recording chamber and superfused (2 ml/min) with recording artificial cerebrospinal fluid (raCSF) composed of (in mM): 126 NaCl, 3 KCl, 1.25 NaH₂PO₄, 2 MgCl₂, 24 D(+)-glucose, 24 NaHCO₃ and 2 CaCl₂ saturated with carbogen at 28–30°C (pH = 7.40; 315–325 mOsm).

Whole cell recordings were from neuronal cell bodies (visualized method (Zeiss Axioskop 2FS microscope) located in the darker, striated region (lamina I) ventral to the outer white matter tracts and dorsal to the substantia gelatinosa, the translucent laminar region that demarcates lamina II (Hildebrand et al., 2014) and were carried out using patch pipettes (5–6 MΩ) containing Cs-gluconate intracellular solution (ICS) composed of (in mM): 105 Cs-gluconate, 17.5 CsCl, 10 HEPES, 10 BAPTA

(Life Technologies), 5 QX-314 (Millipore Sigma), 2 Mg-ATP, 0.3 GTP (pH = 7.20; 290 mOsm) or K-gluconate ICS composed of (in mM): 132.5 K-gluconate, 17.5 KCl, 10 HEPES, 0.2 EGTA, 2.0 Mg-ATP, 0.3 GTP (pH 7.20, 290 mOsm). Patch pipettes were pulled from filament-containing borosilicate glass capillaries (TW150F-4; World Precision Instruments Inc., Sarasota, FL, USA) using a Flaming/Brown Micropipette Puller (Model P-97, Sutter Instruments Co., USA), the tips were fire-polished using a micro forge (model Micro Forge MF-830, Nareshige; Tokyo, Japan), and positioned for recording using a MP-225 Sutter micromanipulator (Sutter Instrument Company).

Data acquired from lamina I neurons included unitary excitatory postsynaptic excitatory postsynaptic currents (μ EPSCs) or unitary excitatory postsynaptic potentials (μ EPSPs) evoked by stimulating a single primary afferent synaptic connection to the lamina I neuron recorded. To isolate activation of an individual synaptic connection between a primary afferent axon and a lamina I neuron, the tip of an in-house designed and constructed (by GMP) fine bipolar stimulating electrode (consisting of two $\sim 50 \mu\text{m}$ diameter single nichrome wire electrodes (A-M Systems, Inc.) separated by $\sim 15 \mu\text{m}$ formvar insulation coating) was placed in the dorsal rootlet entry zone which contains axons of primary afferent neurons that are monosynaptically connected to lamina I neurons. Activation of a putative individual axon at the electrode tip consisted of single pulses of electrical stimulation (0.08 ms duration at 0.2 Hz delivered to the electrode via an S48 Grass Stimulator) with stimulus intensity increased gradually beginning at 0 stimulus intensity (minimal stimulation) until all-or-none unitary postsynaptic responses of the lamina I neuron recorded were detected at which point stimulus intensity (i.e., stimulus threshold) was no longer adjusted (see Results).

μ EPSC recordings acquired from lamina I neurons were voltage-clamped at +60 mV using pipettes containing Cs-gluconate ICS. In most of these voltage-clamp recordings μ EPSCs were also acquired at a holding potential of -65 mV. μ EPSPs were also acquired from lamina I neurons resting at -65 mV using pipettes containing K-gluconate ICS. Of note, prior to acquiring μ EPSPs in a given recording we acquired first in the same recording μ EPSCs in voltage-clamp mode (Vh: -65 mV). Rationale and further details of these experiments are provided in the Results.

In all experiments, raCSF contained [R-(R*,S*)]-5-(6,8-Dihydro-8-oxofuro[3,4-e]-1,3-benzodioxol-6-yl)-5,6,7,8-tetrahydro-6,6-dimethyl-1,3-dioxolo[4,5-g]isoquinolinium chloride (bicuculline methochloride, 10 μM dissolved in H₂O; Tocris Bioscience). The following compounds were added to raCSF as indicated in the Results section: D-(-)-2-Amino-5-phosphonopentanoic acid (D-APV, 100 μM dissolved in H₂O; Tocris Bioscience), (5S,10R)-(+)-5-Methyl-10,11-dihydro-5H-dibenzo[a,d]cyclohepten-5,10-imine maleate (MK-801, 10 μM dissolved in H₂O; Tocris Bioscience), 3-Chloro-4-fluoro-N-[4-[[2-(phenylcarbonyl)hydrazino]carbonyl]benzyl]benzene-sulfonamide (TCN-201, 3 μM dissolved in DMSO; Tocris Bioscience), (α R, β S)- α -(4-Hydroxyphenyl)- β -methyl-4-(phenylmethyl)-1-piperidinepropanol maleate (Ro25-6981, 1 μM dissolved in H₂O; Tocris Bioscience), 5-(4-Bromophenyl)-3-(1,2-dihydro-6-methyl-2-oxo-4-phenyl-3-quinolinyl)-4,5-dihydro- γ -oxo-1H-pyrazole-1-butanoic acid (DQP-1105, 10 μM dissolved in DMSO; Tocris Bioscience), or 6-Cyano-7-nitroquinoxaline-2,3-dione disodium (CNQX, 10 μM dissolved in H₂O; Tocris Bioscience), or

tetrodotoxin (TTX, 0.5 μM dissolved in H₂O; Alomone Labs). Recordings were carried out with the experimenter (GMP) blind to the NMDAR GluN2-selective and non-selective NMDAR inhibitors/blockers tested.

Raw data were amplified using a MultiClamp 700A amplifier and a Digidata 1322A acquisition system sampled at 10 kHz, and analyzed with Clampfit 10.3 (Axon Instruments), Microsoft Office Excel, and Sigmaplot 11 software (Systat Software, Inc.). Junction potential was accounted for in all current-clamp experiments. Data from voltage-clamp experiments were discarded if the series resistance monitored in the recording changed by more than 15%.

Data analysis

Data from minimal stimulation experiments were considered *bona fide* minimal stimulation-elicited unitary postsynaptic responses and used for analysis only if the unitary responses in a given experiment exhibited a clear stimulus threshold (all-or-none postsynaptic events) determined upon increasing gradually stimulation intensity from 0 to the threshold stimulus intensity, a clear unimodal, normal distribution of the events, as well as a consistent latency with each stimulus (see Results). All recordings in every experiment were inspected visually to verify failure and non-failure responses. μ EPSC kinetic parameters measured for analysis (including decay, amplitude, half-width, charge transfer, and rise time) were calculated from the mean μ EPSC trace of all the non-failure responses in that experiment. The decay time constant(s) of the mean μ EPSC (Vh: +60 mV) was calculated in Clampfit by least-squares fitting with one or more exponentials. The best-fit of a given μ EPSC decay was determined by comparing R^2 for the respective fit(s) of that decay. In current-clamp experiments, μ EPSP kinetic parameters including peak amplitude, half-width, and area under the curve were also measured (see Results for details). Failure rate (%) of unitary events in a given minimal stimulation recording was calculated as the percentage of failures that occurred in that given recording.

Statistics

Comparisons between independent groups were carried out by two-tail *t*-test (no equal variance assumed). Comparisons between paired groups were carried out by paired *t*-test, comparisons on repeated measures were performed by repeated measures ANOVA. Significance was established at $\mu = 0.05$, or at a corrected value following Bonferroni correction for multiple comparisons where appropriate. Kinetic data were normalized, scaled and analyzed in R by PCA and HC clustering, followed by gap-statistic to select the optimal number of clusters. HC was built using the euclidean distance method and the Ward linkage method.

Data availability statement

The original contributions presented in this study are included in this article/**Supplementary material**, further inquiries can be directed to the corresponding authors.

Ethics statement

The animal study was reviewed and approved by the Hospital for Sick Children Animal Care Committee.

Author contributions

GP conceived the study, designed the project, conducted the experiments, analyzed the data, and wrote the manuscript. LG carried out statistical analysis and reviewed the manuscript. AM and MT advised on analysis design and reviewed the manuscript. MWS advised on analysis and project design and wrote the manuscript. All authors contributed to the article and approved the submitted version.

Funding

This study was supported by a grant from Canadian Institutes of Health Research (CIHR, FDN-154336) and by the Krembil Foundation to MWS.

Acknowledgments

We thank L. Y. Wang (The Hospital for Sick Children), Steve Prescott (The Hospital for Sick Children), and Stephanie Ratte (The Hospital for Sick Children) for critical reading of the manuscript.

Conflict of interest

The authors declare that the research was conducted in the absence of any commercial or financial relationships that could be construed as a potential conflict of interest.

The reviewer TW declared a shared affiliation, though no other collaboration, with one of the authors LG to the handling editor.

Publisher's note

All claims expressed in this article are solely those of the authors and do not necessarily represent those of their affiliated organizations, or those of the publisher, the editors and the reviewers. Any product that may be evaluated in this article, or claim that may be made by its manufacturer, is not guaranteed or endorsed by the publisher.

Supplementary material

The Supplementary Material for this article can be found online at: <https://www.frontiersin.org/articles/10.3389/fnsyn.2023.1197174/full#supplementary-material>

SUPPLEMENTARY FIGURE 1

Confirmation of minimal stimulation-evoked unitary synaptic responses. **(A)** Scatter plot illustrating minimal stimulation-evoked μ EPSCs (V_h : -65 mV) eliminated by TTX (500 nM). **(B)** Left: Sample traces showing individual traces (V_h : -65 mV), (*i-v*) from **(A)**, demonstrating successful μ EPSCs and failures in response to minimal stimulation (the stimulus artifact is depicted by the gray arrow). A spontaneous EPSC is shown in trace *iii*. Right: Successful μ EPSCs are blocked following TTX administration. μ EPSCs are shown in traces *vi-ix*. **(C)** Scatter plot showing evoked μ EPSCs (V_h : $+60$ mV) at minimal stimulation threshold (gray arrow at left; sample μ EPSCs shown at *i-ii*), and slightly above threshold (thick gray arrow at right) which evoked a second level of all-or-none responses (sample μ EPSCs shown at *iii-iv*). Stimulus intensity below that of minimal stimulation intensity (thin gray arrow at time point 3 min) did not evoke μ EPSCs. **(D)** Paired-pulse minimal stimulation experiment showing average amplitude (\pm SEM) of μ EPSCs (V_h : $+60$ mV) to the second stimulus [*d(ii)*] was greater than that of the first [*d(i)*] when the first stimulus also evoked a μ EPSC. The average amplitude of the μ EPSCs to the second stimulus [*d(iii)*] that followed a failure of response to the first stimulus was also identical, if not greater than, the average amplitude (\pm SEM) of the response to the second stimulus that followed the first stimulus non-failures. Right: *d(i)* scatter plot showing μ EPSC amplitude with a single distribution (insert below) evoked during the first stimulus. *d(ii)* and *d(iii)* show single distributions of μ EPSCs to the second stimulus. **(E)** Same experiment as in (d) but recorded from a different lamina I neuron. Insert above shows that single pulse minimal stimulation evoked a mean (\pm SEM) μ EPSC recorded prior to paired-pulse stimulation (left) is identical to the mean (\pm SEM) μ EPSC recorded in the same experiment but after paired-pulse stimulation (right).

SUPPLEMENTARY FIGURE 2

Additional principal component and hierarchical cluster analysis of the electrophysiological parameters of the μ EPSCs recorded (V_h : $+60$ mV). **(A)** Bi-plot representing the individual data points of the full experimental dataset in the PCA space of the variables in the study. The first two dimensions describe 60% of the dataset variance. **(B)** Heatmap representing the contributions of variables in accounting for the variability in the PCA components. Values are expressed in percentage of the total variability in the PCA components. **(C)** Scatter plot of the raw data color-coded based on HC-defined subtype affiliation.

SUPPLEMENTARY FIGURE 3

Representative fast, intermediate, and slow μ EPSCs. **(A)** Sample trace (black) showing an individual fast decay μ EPSC (V_h : $+60$ mV) from a representative spinal lamina I neuron (gray arrow indicates stimulus artifact). The gray trace shows a synaptic failure. **(B)** Scatter plot of successful synaptic μ EPSCs responses (V_h : $+60$ mV) and failures over time (thick gray bar) evoked by minimal stimulation (0.2 Hz). The thin gray arrow indicates subthreshold stimulation intensity while the thick gray arrow indicates threshold at which μ EPSCs can be evoked. **(C)** NMDAR μ EPSC amplitude histogram showing relative distribution for successful μ EPSCs in this recording **(A,B)**, fit with a single Gaussian function. The NMDAR component of each μ EPSC was measured 30–40 ms after the peak of the μ EPSC. **(D)** Averaged traces (\pm SEM) showing successful μ EPSCs held at $+60$ mV in this recording **(A–C)**. **(E)** Single exponential fitting of the decay component of the averaged μ EPSC in **(D)** held at $+60$ mV. **(F–J)** Recording of a representative intermediate decay μ EPSC (V_h : $+60$ mV) described as per **(A–E)**. **(K–O)** Recording of a representative slow decay μ EPSC (V_h : $+60$ mV) described as per **(A–E)**.

SUPPLEMENTARY FIGURE 4

Multiple representative traces of fast **(A–B)**, intermediate **(C–D)**, and slow **(E–F)** μ EPSCs from recordings in **Supplementary Figure 3** illustrating stable latency, amplitude, and decay.

SUPPLEMENTARY FIGURE 5

D-APV blocks fast, intermediate, and slow μ EPSC decay components. **(A)** Averaged traces (\pm SEM) from a representative recording showing successful fast decay μ EPSCs (V_h : $+60$ mV) before (baseline) and with D-APV (100 mM in aCSF). Averaged traces (\pm SEM) from the same recording showing successful μ EPSCs held at -65 mV. **(B)** Averaged traces (\pm SEM) from a representative recording showing successful intermediate decay μ EPSCs (V_h : $+60$ mV) before (baseline) and with D-APV. Averaged traces (\pm SEM) from the same recording showing successful μ EPSCs held at -65 mV. **(C)** Averaged traces (\pm SEM) from a representative recording showing successful slow decay μ EPSCs (V_h : $+60$ mV) before (baseline) and with D-APV. Averaged traces (\pm SEM) from the same recording showing successful μ EPSCs held at -65 mV with D-APV present.

SUPPLEMENTARY FIGURE 6

Effect of DQP-1105 (10 μ M mM in aCSF) on the decay and charge transfer of fast, intermediate, and slow μ EPSCs. **(A)** Averaged traces (\pm SEM) from a representative recording showing successful slow decay μ EPSCs (Vh: + 60 mv) before (baseline) and with DQP-1105 (gray arrow indicates stimulus artifact). **(B)** Averaged traces (\pm SEM) from a representative recording showing successful intermediate decay μ EPSCs (Vh: + 60 mv) before (baseline) and with DQP-1105. **(C)** Averaged traces (\pm SEM) from a representative recording showing successful fast decay μ EPSCs (Vh: + 60 mv) before (baseline) and with DQP-1105. **(D)** Summary scatter plot showing effect of DQP-1105 on μ EPSC charge transfer from recordings before (baseline) and with DQP-1105 present. **(E)** Summary histogram showing a depressive effect of DQP-1105 on charge transfer of representative slow decay μ EPSCs from **(D)** ($n = 3$; $p < 0.05$ vs. baseline, paired t -test). **(F)** Summary histogram showing no effect of DQP-1105 on charge transfer of representative intermediate decay μ EPSCs from **(D)** ($n = 9$; $p > 0.05$ vs. baseline). **(G)** Summary histogram showing no effect of DQP-1105 on charge transfer of representative fast decay μ EPSCs from **(D)** ($n = 5$; $p > 0.05$ vs. baseline). In panels **(E–G)**, group data are mean \pm SEM.

SUPPLEMENTARY FIGURE 7

Effect of Ro25-6981 (1 μ M in aCSF) on the decay and charge transfer of fast, intermediate, and slow μ EPSCs. **(A)** Averaged traces (\pm SEM) from a representative recording showing successful slow decay μ EPSCs (Vh: + 60 mv) before (baseline) and with Ro25-6981 (gray arrow indicates stimulus artifact). **(B)** Averaged traces (\pm SEM) from a representative recording showing successful intermediate decay μ EPSCs (Vh: + 60 mv) before (baseline) and with Ro25-6981. **(C)** Averaged traces (\pm SEM) from a representative recording showing successful fast decay μ EPSCs (Vh: + 60 mv) before (baseline) and with Ro25-6981. **(D)** Summary scatter plot showing effect of Ro25-6981 on μ EPSC charge transfer from recordings before (baseline) and with Ro25-6981 present. **(E)** Summary histogram showing a partial depressive effect of Ro25-6981 on charge transfer of representative slow decay μ EPSCs from **(D)** ($n = 5$; $p < 0.001$ vs. baseline, paired t -test). **(F)** Summary histogram showing a depressive effect of Ro25-6981 on charge transfer of representative intermediate decay μ EPSCs from **(D)** ($n = 4$; $p < 0.01$ vs. baseline, paired t -test). **(G)** Summary histogram showing no effect of Ro25-6981 on charge transfer of representative fast decay μ EPSCs from **(D)** ($n = 3$; $p > 0.05$ vs. baseline). In panels **(E–G)**, group data are mean \pm SEM.

SUPPLEMENTARY FIGURE 8

Effect of TCN-201 (3 μ M in aCSF) on the decay and charge transfer of fast μ EPSCs. **(A)** Averaged traces (\pm SEM) from a representative recording showing successful fast decay μ EPSCs (Vh: + 60 mv) before and with TCN-201 (gray arrow indicates stimulus artifact). **(B)** Summary scatter plot showing effect of TCN-201 on μ EPSC charge transfer (Vh: + 60 mv) from recordings before (baseline) and with TCN-201 present. **(C)** Summary histogram showing depressive effect of TCN-201 on charge transfer of fast decay μ EPSCs from **(B)** ($n = 3$; $p < 0.01$ vs. baseline, paired t -test). **(D)** Mean (\pm SEM) charge transfer of fast μ EPSCs (Vh: + 60 mv) from **Figure 3A**, represented by (i), is not significantly different from mean (\pm SEM) charge transfer of baseline μ EPSCs held at + 60 mv from panel **"(A)"**, represented by (iii). Mean (\pm SEM) charge transfer of μ EPSCs held at -65 mv from **Figure 3A**, represented by (ii) and considered to be mediated predominantly by AMPAR-mediated charge transfer, is not significantly different from mean (\pm SEM) charge transfer of μ EPSCs held at + 60 mv from panel **"(B)"** with TCN-201 present in aCSF, represented by (iv). **(E)** We reasoned that the difference in charge transfer between (i) and (ii) is the pure fast NMDAR component (white bar), and that the difference in charge transfer between (iii) and (iv) is the pure NMDAR component mediated by GluN2A (red bar). The lack of difference ($p > 0.05$) is therefore interpreted to indicate that the baseline NMDAR component of the fast μ EPSC panels **(A,B)** is mediated exclusively by GluN2A. In panels **(C–E)**, group data are mean \pm SEM.

SUPPLEMENTARY FIGURE 9

Kinetics of μ EPSCs recorded at the holding potential of -65 mv from **Figure 3**. **(A)** Late component of μ EPSCs (Vh: -65 mv) exhibited a significant increase in half-width ($p < 0.01$, unpaired, two-tailed t -test) and charge transfer ($p < 0.05$, 0.01, 0.001, unpaired, two-tailed t -test) across the three groups. The dotted line, full line, the bottom and top of the box, and the whiskers of the plot represent mean, median, lower and upper quartiles, and 10th to 90th percentile, respectively. **(B)** Percent inhibition of the amplitude of the NMDAR component of μ EPSCs held at -65 mv in fast, intermediate, and slow decay groups from **Figure 3**. The percent inhibition of the NMDAR component of μ EPSCs from the "fast" group was similar to that of μ EPSCs from the "intermediate" group, whereas the percent inhibition of the NMDAR component of μ EPSCs from the "slow" group was less. Percent inhibition of the amplitude of the NMDAR component of μ EPSCs held at -65 mv was calculated by dividing the difference between

mean amplitude of the NMDAR component of μ EPSCs held at -65 mv and the mean amplitude of the NMDAR component of μ EPSCs held at + 65 mv by the mean amplitude of the NMDAR component of μ EPSCs held at + 65 mv and multiplying the quotient by 100.

SUPPLEMENTARY FIGURE 10

Lack of effect of NMDAR inhibitors on μ EPSC failure rate. **(A)** Averaged traces (\pm SEM) from a representative recording (at left) showing μ EPSCs (Vh: + 60 mv) before (baseline) and with D-APV (right). Gray arrow indicates stimulus artifact. Below: Scatter plot of successful synaptic μ EPSCs responses (Vh: + 60 mv) and failures over time evoked by minimal stimulation (0.2 Hz). **(B)** Scatter plot showing failure rate (mean \pm SEM) during baseline and with administration of D-APV, TCN-201, Ro25-6981, or DQP-1105 in experiments in which these inhibitors were tested ($n = 46$, $p > 0.05$, paired t -test). **(C)** Scatter plot showing failure rate (mean \pm SEM) during baseline and with administration of D-APV only ($n = 11$, $p > 0.05$, paired t -test).

SUPPLEMENTARY FIGURE 11

μ EPSCs and μ EPSPs recorded sequentially in the same lamina I neuron during a brief train composed of 5 stimuli delivered every 200 ms (5 Hz) at 5 s intervals (0.2 Hz) at minimal stimulation intensity in voltage clamp and then current clamp modes, respectively. **(A)** Mean (\pm SEM) μ EPSC (Vh: -65 mv) trace showing continuous voltage clamp recording during the 5 Hz train (arrows indicate stimulus artifacts throughout the train). Given the continuous nature of these recordings, these traces include both successes and failures. **(B)** Scatter plots (mean \pm SEM; $n = 99$) showing μ EPSC peak amplitude, half-width, charge transfer ($p < 0.001$, non-parametric repeated measures, μ EPSC #1 vs. #5, $p < 0.001$, t -test), and rise time during the 5 Hz train. **(C)** Mean (\pm SEM) μ EPSP trace showing continuous current clamp recording during the 5 Hz train (arrows indicate stimulus artifacts throughout the train). Given the continuous nature of these recordings, these traces include both successes and failures. **(D)** Scatter plots (mean \pm SEM; $n = 100$) showing μ EPSP peak amplitude (non-parametric repeated measures, $p < 0.001$, t -test; μ EPSP #1 vs. #5, $p < 0.001$), half-width (non-parametric repeated measures, $p < 0.001$, t -test; μ EPSP #1 vs. #5, $p < 0.001$), area (non-parametric repeated measures, $p < 0.001$, t -test; μ EPSP #1 vs. #5, $p < 0.001$), and rise time ($p > 0.05$) during the 5 Hz train.

SUPPLEMENTARY FIGURE 12

Pure μ EPSCs (successes only, data extracted from **Supplementary Figure 11A**) shown at each stimulus during the 5 Hz train at minimal stimulation intensity in voltage clamp (Vh: -65 mv). **(A)** Pure mean (\pm SEM) μ EPSC traces (without synaptic failures) shown at each minimal stimulus (arrows indicate stimulus artifacts throughout the train). Representative synaptic failures depicted by the flat traces (mean \pm SEM) are shown at each minimal stimulus. **(B)** Scatter plots (mean \pm SEM) showing μ EPSC peak amplitude ($p > 0.05$, μ EPSC #1 vs. #5), half-width ($p > 0.05$, μ EPSC #1 vs. #5), charge transfer ($p > 0.05$, μ EPSC #1 vs. #5), rise time ($p > 0.05$, μ EPSC #1 vs. #5), and failure rate ($p < 0.05$, non-parametric repeated measures, μ EPSC #1 vs. #5, $p < 0.05$, t -test) for each minimal stimulus.

SUPPLEMENTARY FIGURE 13

Pure μ EPSPs only (successes only, data extracted from **Supplementary Figure 11C**) shown at each stimulus during the 5 Hz train at minimal stimulation intensity in current clamp. **(A)** Pure mean (\pm SEM) μ EPSP traces (without synaptic failures) shown at each minimal stimulus during the 5 Hz train (arrows indicate stimulus artifacts throughout the train). **(B)** Scatter plots (mean \pm SEM) showing μ EPSP peak amplitude ($p < 0.001$, repeated measures ANOVA; μ EPSP #1 vs. #5, $p < 0.001$, t -test), area ($p < 0.001$, μ EPSP #1 vs. #5, $p < 0.001$, statistics as per above), half-width ($p < 0.001$, μ EPSP #1 vs. #5, $p < 0.001$, statistics as per above), rise time ($p > 0.05$, μ EPSP #1 vs. #5), prestimulus membrane potential ($p < 0.001$, μ EPSP #1 vs. #5, $p < 0.001$, statistics as per above), decay ($p < 0.001$, μ EPSP #1 vs. #5, $p < 0.001$, statistics as per above), and failure rate ($p < 0.05$, μ EPSP #1 vs. #5, $p < 0.05$, statistics as per above) for each minimal stimulus.

SUPPLEMENTARY FIGURE 14

Effects of D-APV or MK-801 on μ EPSP bursts. **(A)** Mean (\pm SEM) μ EPSP burst traces showing continuous recording during the 5 Hz train (gray arrows indicate stimulus artifacts throughout the train) during baseline (summed mean \pm SEM trace), with D-APV (100 mM), followed by CNQX (10 mM). Given the continuous nature of these recordings, these traces include successes and failures. **(B)** Mean (\pm SEM) μ EPSP burst traces showing continuous recording during the 5 Hz train (arrows indicate stimulus artifacts throughout the train) during baseline (summed mean \pm SEM trace), with the NMDAR blocker, MK-801 (10 μ M), followed by CNQX (10 mM). Given the continuous nature of these recordings, these traces include successes and failures.

References

- Acker, T. M., Yuan, H., Hansen, K. B., Vance, K. M., Ogden, K. K., Jensen, H. S., et al. (2011). Mechanism for noncompetitive inhibition by novel GluN2C/D N-methyl-D-aspartate receptor subunit-selective modulators. *Mol. Pharmacol.* 80, 782–795. doi: 10.1124/mol.111.073239
- Antal, M., Fukazawa, Y., Eördögh, M., Muszil, D., Molnár, E., Itakura, M., et al. (2008). Numbers, densities, and colocalization of AMPA- and NMDA-type glutamate receptors at individual synapses in the superficial spinal dorsal horn of rats. *J. Neurosci. Off. J. Soc. Neurosci.* 28, 9692–9701. doi: 10.1523/JNEUROSCI.1551-08.2008
- Antic, S. D., Zhou, W.-L., Moore, A. R., Short, S. M., and Ikonomu, K. D. (2010). The decade of the dendritic NMDA spike. *J. Neurosci. Res.* 88, 2991–3001. doi: 10.1002/jnr.22444
- Arellano, J. I., Benavides-Piccione, R., Defelipe, J., and Yuste, R. (2007). Ultrastructure of dendritic spines: Correlation between synaptic and spine morphologies. *Front. Neurosci.* 1:131–143. doi: 10.3389/neuro.01.1.1.010.2007
- Bard, L., Sainlos, M., Bouchet, D., Cousins, S., Mikasova, L., Breillat, C., et al. (2010). Dynamic and specific interaction between synaptic NR2-NMDA receptor and PDZ proteins. *Proc. Natl. Acad. Sci. U.S.A.* 107, 19561–19566. doi: 10.1073/pnas.1002690107
- Bassand, P., Bernard, A., Ra, A., Gayet, D., Khrestchatsky, M., Rene, A., et al. (1999). Differential interaction of the t SXV motifs of the NR1 and NR2A NMDA receptor subunits with PSD-95 and SAP97. *Eur. J. Neurosci.* 11, 2031–2043.
- Bopp, R., Holler-Rickauer, S., Martin, K. A. C., and Schuhknecht, G. F. P. (2017). An ultrastructural study of the thalamic input to Layer 4 of primary motor and primary somatosensory cortex in the mouse. *J. Neurosci. Off. J. Soc. Neurosci.* 37, 2435–2448. doi: 10.1523/JNEUROSCI.2557-16.2017
- Borczyk, M., Śliwińska, M. A., Caly, A., Bernas, T., and Radwanska, K. (2019). Neuronal plasticity affects correlation between the size of dendritic spine and its postsynaptic density. *Sci. Rep.* 9:1693. doi: 10.1038/s41598-018-38412-7
- Broadhead, M. J., Bonthron, C., Arcinas, L., Bez, S., Zhu, F., Goff, F., et al. (2020). Nanostructural diversity of synapses in the mammalian spinal cord. *Sci. Rep.* 10:8189. doi: 10.1038/s41598-020-64874-9
- Broman, J., and Adahl, F. (1994). Evidence for vesicular storage of glutamate in primary afferent terminals. *Neuroreport* 5, 1801–1804. doi: 10.1097/00001756-199409080-00029
- Broman, J., Anderson, S., and Ottersen, O. P. (1993). Enrichment of glutamate-like immunoreactivity in primary afferent terminals throughout the spinal cord dorsal horn. *Eur. J. Neurosci.* 5, 1050–1061. doi: 10.1111/j.1460-9568.1993.tb00958.x
- Browne, T. J., Gradwell, M. A., Iredale, J. A., Maden, J. F., Callister, R. J., Hughes, D. I., et al. (2020). Transgenic cross-referencing of inhibitory and excitatory interneuron populations to dissect neuronal heterogeneity in the dorsal horn. *Front. Mol. Neurosci.* 13:32. doi: 10.3389/fnmol.2020.00032
- Chen, X., Levy, J. M., Hou, A., Winters, C., Azzam, R., Sousa, A. A., et al. (2015). PSD-95 family MAGUKs are essential for anchoring AMPA and NMDA receptor complexes at the postsynaptic density. *Proc. Natl. Acad. Sci. U.S.A.* 112, E6983–E6992. doi: 10.1073/pnas.1517045112
- Cizeron, M., Qiu, Z., Koniaris, B., Gokhale, R., Komiyama, N. H., Fransén, E., et al. (2020). A brainwide atlas of synapses across the mouse life span. *Science* 369, 270–275. doi: 10.1126/science.aba3163
- Clarke, R. J., and Johnson, J. W. (2006). NMDA receptor NR2 subunit dependence of the slow component of magnesium unblock. *J. Neurosci. Off. J. Soc. Neurosci.* 26, 5825–5834. doi: 10.1523/JNEUROSCI.0577-06.2006
- Coba, M. P., Pocklington, A. J., Collins, M. O., Kopanitsa, M. V., Uren, R. T., Swamy, S., et al. (2009). Neurotransmitters drive combinatorial multistate postsynaptic density networks. *Sci. Signal.* 2:ra19. doi: 10.1126/scisignal.2000102
- Collins, M. O., Husi, H., Yu, L., Brandon, J. M., Anderson, C. N. G., Blackstock, W. P., et al. (2006). Molecular characterization and comparison of the components and multiprotein complexes in the postsynaptic proteome. *J. Neurochem.* 97(Suppl 1), 16–23. doi: 10.1111/j.1471-4159.2005.03507.x
- Cousins, S. L., and Stephenson, F. A. (2012). Identification of N-methyl-D-aspartic acid (n.d.) receptor subtype-specific binding sites that mediate direct interactions with scaffold protein PSD-95. *J. Biol. Chem.* 287, 13465–13476. doi: 10.1074/jbc.M111.292862
- Cousins, S. L., Kenny, A. V., and Stephenson, F. A. (2009). Delineation of additional PSD-95 binding domains within NMDA receptor NR2 subunits reveals differences between NR2A/PSD-95 and NR2B/PSD-95 association. *Neuroscience* 158, 89–95. doi: 10.1016/j.neuroscience.2007.12.051
- Cousins, S. L., Papadakis, M., Rutter, A. R., and Stephenson, F. A. (2008). Differential interaction of NMDA receptor subtypes with the post-synaptic density-95 family of membrane associated guanylate kinase proteins. *J. Neurochem.* 104, 903–913. doi: 10.1111/j.1471-4159.2007.05067.x
- Cull-Candy, S. G., and Leszkiewicz, D. N. (2004). Role of distinct NMDA receptor subtypes at central synapses. *Sci. STKE* 2004:re16. doi: 10.1126/stke.2552004re16
- Enoki, R., Kiuchi, T., Koizumi, A., Sasaki, G., Kudo, Y., and Miyakawa, H. (2004). NMDA receptor-mediated depolarizing after-potentials in the basal dendrites of CA1 pyramidal neurons. *Neurosci. Res.* 48, 325–333. doi: 10.1016/j.neures.2003.11.011
- Fischer, G., Mutel, V., Trube, G., Malherbe, P., Kew, J. N., Mohacs, E., et al. (1997). Ro 25-6981, a highly potent and selective blocker of N-methyl-D-aspartate receptors containing the NR2B subunit. Characterization *in vitro*. *J. Pharmacol. Exp. Ther.* 283, 1285–1292.
- Frank, R. A. W., Komiyama, N. H., Ryan, T. J., Zhu, F., O'Dell, T. J., and Grant, S. G. N. (2016). NMDA receptors are selectively partitioned into complexes and supercomplexes during synapse maturation. *Nat. Commun.* 7:11264. doi: 10.1038/ncomms11264
- Frank, R. A. W., Zhu, F., Komiyama, N. H., and Grant, S. G. N. (2017). Hierarchical organization and genetically separable subfamilies of PSD95 postsynaptic supercomplexes. *J. Neurochem.* 142, 504–511. doi: 10.1111/jnc.14056
- Frank, R. A., and Grant, S. G. (2017). Supramolecular organization of NMDA receptors and the postsynaptic density. *Curr. Opin. Neurobiol.* 45, 139–147. doi: 10.1016/j.conb.2017.05.019
- Froemke, R. C., Letzkus, J. J., Kampa, B. M., Hang, G. B., Stuart, G. J., and Surmeier, D. J. (2010). Dendritic synapse location and neocortical spike-timing-dependent plasticity. *Front. Synaptic Neurosci.* 2:29. doi: 10.3389/fnsyn.2010.00029
- Gao, P. P., Graham, J. W., Zhou, W.-L., Jang, J., Angulo, S., Dura-Bernal, S., et al. (2021). Local glutamate-mediated dendritic plateau potentials change the state of the cortical pyramidal neuron. *J. Neurophysiol.* 125, 23–42. doi: 10.1152/jn.00734.2019
- Gardoni, F., and Di Luca, M. (2021). Protein-protein interactions at the NMDA receptor complex: From synaptic retention to synaptonuclear protein messengers. *Neuropharmacology* 190:108551. doi: 10.1016/j.neuropharm.2021.108551
- Goncalves, J., Bartol, T. M., Camus, C., Levét, F., Menegolla, A. P., Sejnowski, T. J., et al. (2020). Nanoscale co-organization and coactivation of AMPAR, NMDAR, and mGluR at excitatory synapses. *Proc. Natl. Acad. Sci. U.S.A.* 117, 14503–14511. doi: 10.1073/pnas.1922563117
- González-Burgos, G., and Barrionuevo, G. (2001). Voltage-gated sodium channels shape subthreshold EPSPs in layer 5 pyramidal neurons from rat prefrontal cortex. *J. Neurophysiol.* 86, 1671–1684. doi: 10.1152/jn.2001.86.4.1671
- Grant, S. G. N., and Fransén, E. (2020). The Synapse diversity dilemma: Molecular heterogeneity confounds studies of synapse function. *Front. Synaptic Neurosci.* 12:590403. doi: 10.3389/fnsyn.2020.590403
- Gray, N. W., Weimer, R. M., Bureau, I., and Svoboda, K. (2006). Rapid redistribution of synaptic PSD-95 in the neocortex *in vivo*. *PLoS Biol.* 4:e370. doi: 10.1371/journal.pbio.0040370
- Hansen, K. B., Ogden, K. K., and Traynelis, S. F. (2012). Subunit-selective allosteric inhibition of glycine binding to NMDA receptors. *J. Neurosci. Off. J. Soc. Neurosci.* 32, 6197–6208. doi: 10.1523/JNEUROSCI.5757-11.2012
- Häring, M., Zeisel, A., Hochgerner, H., Rinwa, P., Jakobsson, J. E. T., Lönnerberg, P., et al. (2018). Neuronal atlas of the dorsal horn defines its architecture and links sensory input to transcriptional cell types. *Nat. Neurosci.* 21, 869–880. doi: 10.1038/s41593-018-0141-1
- Hildebrand, M. E., Pitcher, G. M., Harding, E. K., Li, H., Beggs, S., and Salter, M. W. (2014). GluN2B and GluN2D NMDARs dominate synaptic responses in the adult spinal cord. *Sci. Rep.* 4:4094. doi: 10.1038/srep04094
- Holler, S., Köstinger, G., Martin, K. A. C., Schuhknecht, G. F. P., and Stratford, K. J. (2021). Structure and function of a neocortical synapse. *Nature* 591, 111–116. doi: 10.1038/s41586-020-03134-2
- Holtmaat, A., and Svoboda, K. (2009). Experience-dependent structural synaptic plasticity in the mammalian brain. *Nat. Rev. Neurosci.* 10, 647–658. doi: 10.1038/nrn2699
- Hruska, M., Cain, R. E., and Dalva, M. B. (2022). Nanoscale rules governing the organization of glutamate receptors in spine synapses are subunit specific. *Nat. Commun.* 13:920. doi: 10.1038/s41467-022-28504-4
- Kellermayer, B., Ferreira, J. S., Dupuis, J., Levét, F., Grillo-Bosch, D., Bard, L., et al. (2018). Differential nanoscale topography and functional role of GluN2-NMDA receptor subtypes at glutamatergic synapses. *Neuron* 100, 106–119.e7. doi: 10.1016/j.neuron.2018.09.012
- Kharazia, V. N., and Weinberg, R. J. (1997). Tangential synaptic distribution of NMDA and AMPA receptors in rat neocortex. *Neurosci. Lett.* 238, 41–44. doi: 10.1016/s0304-3940(97)00846-x
- Kilinc, D. (2018). The emerging role of mechanics in synapse formation and plasticity. *Front. Cell. Neurosci.* 12:483. doi: 10.3389/fncel.2018.00483
- Konur, S., Rabinowitz, D., Fenstermaker, V. L., and Yuste, R. (2003). Systematic regulation of spine sizes and densities in pyramidal neurons. *J. Neurobiol.* 56, 95–112. doi: 10.1002/neu.10229

- Kornau, H. C., Schenker, L. T., Kennedy, M. B., and Seeburg, P. H. (1995). Domain interaction between NMDA receptor subunits and the postsynaptic density protein PSD-95. *Science* 269, 1737–1740. doi: 10.1126/science.7569905
- Kumar, A., Schiff, O., Barkai, E., Mel, B. W., Poleg-Polsky, A., and Schiller, J. (2018). NMDA spikes mediate amplification of inputs in the rat piriform cortex. *Elife* 7:e38446. doi: 10.7554/eLife.38446
- Kuner, T., and Schoepfer, R. (1996). Multiple structural elements determine subunit specificity of Mg²⁺ block in NMDA receptor channels. *J. Neurosci. Off. J. Soc. Neurosci.* 16, 3549–3558. doi: 10.1523/JNEUROSCI.16-11-03549.1996
- Lavzin, M., Rapoport, S., Polsky, A., Garion, L., and Schiller, J. (2012). Nonlinear dendritic processing determines angular tuning of barrel cortex neurons in vivo. *Nature* 490, 397–401. doi: 10.1038/nature11451
- Li, C., and Gullledge, A. T. (2021). NMDA receptors enhance the fidelity of synaptic integration. *eNeuro* 8, 1–19. doi: 10.1523/ENEURO.0396-20.2020
- Lin, Y., Skeberdis, V. A., Francesconi, A., Bennett, M. V. L., and Zukin, R. S. (2004). Postsynaptic density protein-95 regulates NMDA channel gating and surface expression. *J. Neurosci. Off. J. Soc. Neurosci.* 24, 10138–10148. doi: 10.1523/JNEUROSCI.3159-04.2004
- Losi, G., Prybylowski, K., Fu, Z., Luo, J., Wenthold, R. J., and Vicini, S. (2003). PSD-95 regulates NMDA receptors in developing cerebellar granule neurons of the rat. *J. Physiol.* 548, 21–29. doi: 10.1113/jphysiol.2002.034918
- Manita, S., Miyazaki, K., and Ross, W. N. (2011). Synaptically activated Ca²⁺ waves and NMDA spikes locally suppress voltage-dependent Ca²⁺ signalling in rat pyramidal cell dendrites. *J. Physiol.* 589, 4903–4920. doi: 10.1113/jphysiol.2011.216564
- Matsumoto, M., Inoue, M., Hald, A., Yamaguchi, A., and Ueda, H. (2006). Characterization of three different sensory fibers by use of neonatal capsaicin treatment, spinal antagonism and a novel electrical stimulation-induced paw flexion test. *Mol. Pain* 2:16. doi: 10.1186/1744-8069-2-16
- Matsuzaki, M., Honkura, N., Ellis-Davies, G. C. R., and Kasai, H. (2004). Structural basis of long-term potentiation in single dendritic spines. *Nature* 429, 761–766. doi: 10.1038/nature02617
- Menon, V., Musial, T. F., Liu, A., Katz, Y., Kath, W. L., Spruston, N., et al. (2013). Balanced synaptic impact via distance-dependent synapse distribution and complementary expression of AMPARs and NMDARs in hippocampal dendrites. *Neuron* 80, 1451–1463. doi: 10.1016/j.neuron.2013.09.027
- Otor, Y., Achvat, S., Cermak, N., Benisty, H., Abboud, M., Barak, O., et al. (2022). Dynamic compartmental computations in tuft dendrites of layer 5 neurons during motor behavior. *Science* 376, 267–275. doi: 10.1126/science.abn1421
- Palmer, L. M., Shai, A. S., Reeve, J. E., Anderson, H. L., Paulsen, O., and Larkum, M. E. (2014). NMDA spikes enhance action potential generation during sensory input. *Nat. Neurosci.* 17, 383–390. doi: 10.1038/nn.3646
- Paoletti, P., Bellone, C., and Zhou, Q. (2013). NMDA receptor subunit diversity: impact on receptor properties, synaptic plasticity and disease. *Nat. Rev. Neurosci.* 14, 383–400. doi: 10.1038/nrn3504
- Pitcher, G. M., Kalia, L. V., Ng, D., Goodfellow, N. M., Yee, K. T., Lambe, E. K., et al. (2011). Schizophrenia susceptibility pathway neuregulin 1-ErbB4 suppresses Src upregulation of NMDA receptors. *Nat. Med.* 17, 470–478. doi: 10.1038/nm.2315
- Plotkin, J. L., Day, M., and Surmeier, D. J. (2011). Synaptically driven state transitions in distal dendrites of striatal spiny neurons. *Nat. Neurosci.* 14, 881–888. doi: 10.1038/nn.2848
- Poleg-Polsky, A. (2015). Effects of neural morphology and input distribution on synaptic processing by global and focal NMDA-spikes. *PLoS One* 10:e0140254. doi: 10.1371/journal.pone.0140254
- Prescott, S. A., and De Koninck, Y. (2005). Integration time in a subset of spinal lamina I neurons is lengthened by sodium and calcium currents acting synergistically to prolong subthreshold depolarization. *J. Neurosci. Off. J. Soc. Neurosci.* 25, 4743–4754. doi: 10.1523/JNEUROSCI.0356-05.2005
- Punnakkal, P., von Schoultz, C., Haenraets, K., Wildner, H., and Zeilhofer, H. U. (2014). Morphological, biophysical and synaptic properties of glutamatergic neurons of the mouse spinal dorsal horn. *J. Physiol.* 592, 759–776. doi: 10.1113/jphysiol.2013.264937
- Racca, C., Stephenson, F. A., Streit, P., Roberts, J. D., and Somogyi, P. (2000). NMDA receptor content of synapses in stratum radiatum of the hippocampal CA1 area. *J. Neurosci. Off. J. Soc. Neurosci.* 20, 2512–2522. doi: 10.1523/JNEUROSCI.20-07-02512.2000
- Roy, M., Sorokina, O., McLean, C., Tapia-González, S., DeFelipe, J., Armstrong, J. D., et al. (2018a). Regional diversity in the postsynaptic proteome of the mouse brain. *Proteomes* 6:31. doi: 10.3390/proteomes6030031
- Roy, M., Sorokina, O., Skene, N., Simonnet, C., Mazzo, F., Zwart, R., et al. (2018b). Proteomic analysis of postsynaptic proteins in regions of the human neocortex. *Nat. Neurosci.* 21, 130–138. doi: 10.1038/s41593-017-0025-9
- Schiller, J., and Schiller, Y. (2001). NMDA receptor-mediated dendritic spikes and coincident signal amplification. *Curr. Opin. Neurobiol.* 11, 343–348. doi: 10.1016/s0959-4388(00)00217-8
- Schiller, J., Major, G., Koester, H. J., and Schiller, Y. (2000). NMDA spikes in basal dendrites of cortical pyramidal neurons. *Nature* 404, 285–289. doi: 10.1038/35005094
- Scholl, B., Thomas, C. I., Ryan, M. A., Kamasawa, N., and Fitzpatrick, D. (2021). Cortical response selectivity derives from strength in numbers of synapses. *Nature* 590, 111–114. doi: 10.1038/s41586-020-03044-3
- Shinohara, Y., and Hirase, H. (2009). Size and receptor density of glutamatergic synapses: A viewpoint from left–right asymmetry of CA3–CA1 connections. *Front. Neuroanat.* 3:10. doi: 10.3389/neuro.05.010.2009
- Shiokawa, H., Kaftan, E. J., MacDermott, A. B., and Tong, C.-K. (2010). NR2 subunits and NMDA receptors on lamina II inhibitory and excitatory interneurons of the mouse dorsal horn. *Mol. Pain* 6:26. doi: 10.1186/1744-8069-6-26
- Siegler Retchless, B., Gao, W., and Johnson, J. W. (2012). A single GluN2 subunit residue controls NMDA receptor channel properties via intersubunit interaction. *Nat. Neurosci.* 15, 406–413, S1–S2. doi: 10.1038/nn.3025
- Statman, A., Kaufman, M., Minerbi, A., Ziv, N. E., and Brenner, N. (2014). Synaptic size dynamics as an effectively stochastic process. *PLoS Comput. Biol.* 10:e1003846. doi: 10.1371/journal.pcbi.1003846
- Todd, A. J., Hughes, D. I., Polgár, E., Nagy, G. G., Mackie, M., Ottersen, O. P., et al. (2003). The expression of vesicular glutamate transporters VGLUT1 and VGLUT2 in neurochemically defined axonal populations in the rat spinal cord with emphasis on the dorsal horn. *Eur. J. Neurosci.* 17, 13–27. doi: 10.1046/j.1460-9568.2003.02406.x
- Tong, C.-K., and MacDermott, A. B. (2014). Synaptic GluN2A and GluN2B containing NMDA receptors within the superficial dorsal horn activated following primary afferent stimulation. *J. Neurosci. Off. J. Soc. Neurosci.* 34, 10808–10820. doi: 10.1523/JNEUROSCI.0145-14.2014
- Tong, C.-K., Kaftan, E. J., and Macdermott, A. B. (2008). Functional identification of NR2 subunits contributing to NMDA receptors on substance P receptor-expressing dorsal horn neurons. *Mol. Pain* 4:44. doi: 10.1186/1744-8069-4-44
- Valtschanoff, J. G., Burette, A., Wenthold, R. J., and Weinberg, R. J. (1999). Expression of NR2 receptor subunit in rat somatic sensory cortex: Synaptic distribution and colocalization with NR1 and PSD-95. *J. Comp. Neurol.* 410, 599–611.
- Weber, J. P., Andrásfalvy, B. K., Polito, M., Magó, Á., Ujfalussy, B. B., and Makara, J. K. (2016). Location-dependent synaptic plasticity rules by dendritic spine cooperativity. *Nat. Commun.* 7:11380. doi: 10.1038/ncomms11380
- Yasaka, T., Tiong, S. Y. X., Hughes, D. I., Riddell, J. S., and Todd, A. J. (2010). Populations of inhibitory and excitatory interneurons in lamina II of the adult rat spinal dorsal horn revealed by a combined electrophysiological and anatomical approach. *Pain* 151, 475–488. doi: 10.1016/j.pain.2010.08.008
- Zhu, F., Cizeron, M., Qiu, Z., Benavides-Piccione, R., Kopanitsa, M. V., Skene, N. G., et al. (2018). Architecture of the mouse brain synaptome. *Neuron* 99, 781–799.e10. doi: 10.1016/j.neuron.2018.07.007